COMPUTATIONAL STUDY OF EDGE STABILITY AND TOPOLOGICAL EDGE STATES OF TWO-DIMENSIONAL CARBONIC MATERIALS

by

Ninghai Su

A dissertation submitted to the faculty of
The University of Utah
in partial fulfillment of the requirements for the degree of

Doctor of Philosophy

Department of Materials Science and Engineering

The University of Utah

August 2014

The University of Utah Graduate School

STATEMENT OF DISSERTATION APPROVAL

The dissertation of **Ninghai Su**

has been approved by the following supervisory committee members:

Feng Liu	, Chair	**04/30/2014** Date Approved
Michael Scarpulla	, Member	**04/30/2014** Date Approved
Gerald B. Stringfellow	, Member	**04/30/2014** Date Approved
Ashutosh Tiwari	, Member	**04/30/2014** Date Approved
Ling Zang	, Member	**04/30/2014** Date Approved

and by **Feng Liu** , Chair of

the Department of **Materials Science and Engineering**

and by David B. Kieda, Dean of The Graduate School.

ABSTRACT

In this dissertation, our aim is to contribute to the understanding of edge properties of two-dimensional (2D) carbonic materials, including graphene and organometallic frameworks. A set of modeling and simulations, using first-principles density functional theory (DFT), tight-binding (TB) method, and molecular dynamics (MD) method, have been performed to (1) investigate the structural edge stability of graphene from both thermodynamic and kinetic points of view and (2) explore the existence of nontrivial electronic edge states, which carry nonzero topological invariant, in 2D organometallic frameworks. Specifically, this dissertation comprises the following four chapters of topics: (1) chemical versus thermal folding of graphene edges; (2) quantum manifestations of graphene edge stress and edge instability; (3) prediction of a two-dimensional organic topological insulator; (4) prediction of a large gap flat Chern band in a two-dimensional organic framework. Our work presented in the first two chapters not only has explained certain experimental observations on graphene edges, but also has been confirmed by other researchers' findings, both experimentally and theoretically. The studies shown in the last two chapters predict the existence of quantum spin Hall phase, a physical phenomenon that has been an exciting area of recent research in condensed matter physics, in 2D organometallic frameworks, a class of materials that are used to be mostly of interest to chemists. Therefore, we hope that these new findings could lead to a marriage of condensed matter physics and organic chemistry to foster an interdisciplinary research field, which will broaden the scientific and technology impact of topological materials.

CONTENTS

LIST OF FIGURES

LIST OF TABLES

ACKNOWLEDGMENTS

First and foremost, I thank my supervisor Prof. Feng Liu for his guidance, inspiration, and support during my entire Ph.D. study. He has taught me how to think creatively, pose questions, and express ideas in a scientific manner. Also, he has always been willing to correct mistakes in my research and encourage me to try my own ideas. It has been my great honor and privilege to work with him.

I would like to thank all of my colleagues in Prof. Liu's group for their support and many interesting and helpful discussions, especially Zhengfei Wang, Chao Hui, Miao Liu, and Wenmei Ming. I thank Zhengfei Wang for collaboration and for patiently explaining to me many technical details in the field of solid state physics. I also appreciate my fellow friends, in particular, Miao Liu, Lei Zhang, Jiajia Tan, Kelin Li, Zhe Li, and Fangjian Guo. The many happy hours we spent together made my life balanced over the years in Salt Lake City.

I would like to thank my Ph.D. committee members, Prof. Scarpulla, Prof. Stringfellow, Prof. Tiwari, and Prof. Zang, for donating their valuable time to review my dissertation and attend the dissertation defense. I also thank our departmental administration for helping me with many logistical issues associate with my graduate study.

I want to express special thanks to my beloved Siyuan. She has been standing beside me for the past few years and made my life better. Her endless support and encouragement was in the end what made this dissertation possible. Finally, my mother Qiuping Li and father Zhongmin Su receive my deepest gratitude for their long-time support in my growth and development.

CHAPTER 1

INTRODUCTION TO EDGE STABILITY OF GRAPHENE AND TOPOLOGICAL EDGE STATE OF 2D MATERIALS

1.1 Introduction

Graphene is the first stable, truly two-dimensional (2D) material system consisting of a single layer of carbon atoms arranged in a hexagonal lattice. It attracted tremendous attention right after the first relatively large isolated graphene sheet was peeled off from graphite by using a Scotch-tape [1,2]. As a new playground for researchers with different backgrounds, its stability is fundamental and critical. Within the past few years, many results have been accumulated to approach the stability of graphene from different perspectives, which fall into the two general types: long-range crystalline order in 2D structure and stability of the free edges. As the first 2D membrane structure with only one atomic layer of thickness ever known to mankind [2], graphene provides an ideal testbed [3,4] for the classical Mermin-Wagner theorem on the existence of long-range crystalline order in 2D [5-7]. As the thinnest and strongest object ever obtained [8], graphene also becomes the best specimen to study the stability of the free edges of 2D nano-structures. Moreover, identifying unprecedented electronic properties of graphene is not only of scientific interest but also of technological significance. Graphene could be well described by a simple tight binding (TB) model with the nearest-neighbor hopping on a hexagonal lattice. By solving this TB model, the $E - k$ relation is found to be conically linear around six Dirac points (three K and K' points each) and form the so-called Dirac cone. Electrons and holes within the Dirac cone are called Dirac fermions, which are massless just like photons. The massless Dirac fermions [2,9,10], together with superior thermal [11] and electrical [12] conductance, enable graphene to be promising for many applications. On the other hand, through study of nontrivial topological states in graphene, Kane and Mele established the theoretical foundation for a 2D topological insulator or quantum spin Hall (QSH) phase [13,14]. Their

work has started a totally new research field of topological insulators in condensed matter physics. However, people later found that the QSH effect in graphene is too small to be observed in experiment due to a very weak spin-orbit coupling (SOC) of carbon atoms [15-19]. To overcome this problem, our research group led by Prof. Liu at University of Utah has recently used metal ions with strong SOC and organic ligands to reassemble the 2D atomic layer thick structure of graphene and proposed the concept of a 2D organic topological insulator (OTI) [20-22]. These proposed 2D OTIs were predicted to have robust topological states at their edges and high tunability. In the following part of this chapter, more detailed information about the edge stability of graphene and the topological edge states in the graphene-like 2D organometallic framework will be provided. Anyone who wishes to go into depth of graphene and topological insulators is recommended to read several excellent review articles [23-26].

1.2 Edge Stability of Graphene

The early work done by Landau, Mermin, and Wagner [5-7] has revealed that both crystallographic and magnetic long-range ordering in a 2D lattice is theoretically impossible at any finite temperature. In order to stabilize a 2D lattice, flexural phonons or out-of-plane displacements must be present [3]. Some recent attention has also been paid to the relation between the structural stability and electronic properties of graphene and people found that electronic properties of graphene strongly depend on the morphology of graphene [27-29], especially the structural properties of graphene edges [30-35].

As an ultrathin 2D structure only one atom thick, graphene has low bending rigidity. The edges of suspended graphene could generally warp and fold easily due to large out-of-plane thermal fluctuations at finite temperature [4,35-38]. Graphene with a folded edge could have enhanced electronic conductivity [35] or exhibit quantum Hall (QH) phase [39]. Suspended graphene synthesized in experiments usually has this folded edge structure. A suspended free-standing graphene edge has been observed by transmission electron microscopy (TEM) to fold over, forming a structure similar to one-half of a single-walled carbon nanotube (SWCNT) [4,36]. Using high-resolution TEM, Liu et al. [38] have further shown that both armchair and zigzag edges of graphene exhibit a folded edge state. Moreover, *in situ* observation of multilayer graphene has demonstrated that both the armchair and zigzag edges can form folded structures spontaneously at about 2400 K [37]. On the other hand, a theoretical study using a coarse-grained hierarchical multiscale model has shown that the folded edges are thermodynamically stable beyond a critical folded length [40], and a kinetic

Monte Carlo simulation was consistent with the observed spontaneous folding process at high temperature (∼2400 K) [37].

Moreover, the edges of graphene are under intrinsic nonzero edge stress and can also be externally stressed, either stretched [8,41-45] or compressed [46], and form rippled structure [47]. Effects of strain within graphene edges is equivalent to that of a local magnetic field [48-50], which could play an important role in the transport properties of graphene [39,51] and introduce QH phase into graphene [52]. These results indicate that one could utilize strain to tune the properties of graphene. However, due to the one atomic layer thickness, graphene undergoes buckling instability under compressive stress [53]; on the other hand; it is the strongest material in the world and could sustain extremely large tensile strain without breaking [8].

1.3 Topological Edge States in 2D Organometallic Frameworks

Usually, quantum states of matter, i.e., superconductor and magnetic order, can be described by some of their general properties, i.e., dimensionality and symmetry of order parameter. This principle is called the Landau-Ginzburg theory in condensed matter physics. However, the new quantum state discovered in 1980, which is called the QH state, posed a question about the generality of the Landau-Ginzburg theory. In the experiment conducted by von Klitzing et al. [54], the two-dimensional electron gas in a strong magnetic field showed a precise quantization of Hall conductance

$$\sigma_{xy} = N\frac{e^2}{h} \tag{1.1}$$

on the edges while it is insulating in the bulk. In this system, the quantization of the cyclotron orbits of electrons results in the famous Landau quantization, in which the energy can be expressed as the following quantized form

$$E_n = (n + 1/2)\hbar\omega_c \tag{1.2}$$

where ω_c is the cyclotron frequency. When only the N Landau levels are filled, an energy gap separating occupied and empty states would occur, which leads to an insulator. However, if such a system has an external electric filed applied, then the cyclotron orbits would deform and result in metallic edges with the quantized conductance as described above.

This system is different from the ordinary insulator and cannot be described within the Landau-Ginzburg theory and was later explained by Thouless et al. [55] by linking the Hall conductivity, which is given by the Kubo formula, and a topological invariant, which is called the Chern number. In mathematics, the Chern number is used to answer the question of whether two ostensibly different vector bundles are the same or not. This can be understood in analogy to the genus of 2D orientable surface g, which represents the maximum number of cutting along nonintersecting closed simple curves without rendering the resultant manifold disconnected. For example, a disc has g=0, while a coffee mug with a handle, has g=1. Genus of a surface will sustain unless a hole closes or opens on it. It turns out that we can understand the Chern number physically in the picture of the Berry phase [56] of the electron wavefunctions in the reciprocal space. By integrating the Berry curvature around the entire Brillouin zone, the Chern number should take integer values in units of e^2/h, independent of material details. Also, unless a bandgap closes or opens, the Chern number will not change with the variation of a Hamiltonian.

In order to realize QH phase in a material without net magnetic field applied, Haldane [57] proposed a model and applied it to the lattice of graphene, which was called single layer graphite at that time in 1988, and found nonzero Hall conductance in the lattice. The basic idea in Haldane's model is to break the time reversal symmetry in order to lift the degeneracy at the Dirac point. By including next-nearest-neighbor hopping, a gap is introduced to the graphene lattice by breaking the time reversal symmetry and a QH state was then established.

Then, after the experimental discovery of graphene [1], Kane and Mele [14] revisited the Haldane model and imagined a new situation that the time reversal symmetry restored but with the spin included. In a gapped system with time reversal symmetry, which exhibits a smoothly deformable but nonzero energy gap and a Chern number of zero, the existence of an edge state inside the gap should meet the requirement of the Kramers' theorem that all eigenstates at point k=0 and k=π/a, which are called the time reversal symmetry invariant momenta, should have at least twofold degeneracy. For such a system without SOC, the requirement of the Kramers' theorem is always satisfied because states with different spins are degenerate. But for such a system with SOC, the degeneracy will be lifted at these two points mentioned above. Pairs of these separated states are called Kramers pairs. If there is only one Kramers pair, the edge states of spin-up and spin-down cannot open a gap without violating the Kramer's theorem and will form a 1D Dirac cone within the bulk gap. But if there are two Kramers pairs, the edge states of spin-up and spin-down are

fourfold degenerated at the k=0 point. After opening a gap at this point, the requirement of degeneracy is still fulfilled. Therefore, the time-reversal-symmetry-conserved systems with odd or even Kramers pairs can be characterized by a new topological invariant with 1 or 0, respectively, which is called the $\mathbb{Z}_2$ number. Sheng et al. [58] demonstrated that, for a 2D topological insulator with perpendicular spin, its Chern number, which is defined as the sum of Chern integers for both spin-up and spin-down bands, must be zero in order to protect the time reversal symmetry. But the spin Chern number, which is defined as the difference between the Chern integers, has a nonzero value. This rule could be used to identify 2D topological insulators from the ordinary insulators.

The Kane-Mele model [14] indicates that graphene should host the QSH phase. However, as mentioned above, carbon has very weak SOC, which results in unobservable QSH effect in graphene. To enhance the QSH effect in graphene, one obvious method is to introduce a heavy metallic element into graphene either by substitution or insertion. But it is very difficult, if not impossible, to synthesize such a 2D structure with adequate concentration of heavy metal atoms. Recently, the concept of OTI was proposed by our group [20-22,59], in which heavy metal atoms are linked by planar organic (carbonic) ligands to form well-crystallized 2D structure. The existence of nontrivial edge states inside the SOC gap [21,22] and flat Chern band [20] is theoretically demonstrated in 2D organometallic frameworks formed by metal atoms and benzene rings. A recent experimentally synthesized organometallic framework [60] is also predicted to be an OTI [59].

1.4 Summary

This dissertation is organized as follows. In Chapter 2, we present results of MD simulation of the edge folding process of both suspended single-layer (SLG) and double-layer graphene (DLG). In this study, we have investigated the kinetics of the graphene edge folding process. The lower limit of the energy barrier is found to be 380 meV/Å (or about 800 meV per edge atom) and 50 meV/Å (or about 120 meV per edge atom) for folding the edges of intrinsic clean SLG and DLG, respectively. However, the edge folding barriers can be substantially reduced by imbalanced chemical adsorption, such as of H atoms, on the two sides of graphene along the edges. Our studies indicate that thermal folding is not feasible at room temperature (RT) for clean SLG and DLG edges and is feasible at high temperature only for DLG edges, whereas chemical folding (with adsorbates) of both SLG and DLG edges can be spontaneous at RT. These findings suggest that the folded edge structures of suspended graphene observed in some experiments are possibly due to the

presence of adsorbates at the edges.

In Chapter 3, we further investigate the effects of quantum electronic edge stress on the stability of graphene edge, which provides new insights to the understanding of mechanical stability of graphene in addition to the prior study using the classical MD method. We have performed first-principles calculations of graphene edge stresses, which display two interesting quantum manifestations absent from the classical interpretation: the armchair edge stress oscillates with a nanoribbon width, and the zigzag edge stress is noticeably reduced by spin polarization. Such quantum stress effects in turn manifest in mechanical edge twisting and warping instability, showing features not captured by empirical potentials or continuum theory. Edge adsorption of H and Stone-Wales reconstruction is shown to provide alternative mechanisms in relieving the edge compression and hence to stabilize the planar edge structure.

In Chapter 4, we predict the existence of novel quantum transport properties at the edge of a newly synthesized π-conjugated carbonic 2D lattice. TIs are a class of materials exhibiting unique quantum transport properties with potential applications in spintronics and quantum computing. To date, all of the experimentally confirmed TIs are inorganic materials. Recent theories predicted the possible existence of OTI in 2D organometallic frameworks. However, those theoretically proposed structures do not naturally exist and remain to be made in experiments. Here, we identify a recent experimentally made 2D organometallic framework, consisting of π-conjugated nickel-bis-dithiolene with a chemical formula $Ni_3C_{12}S_{12}$, which exhibits nontrivial topological states in both a Dirac band and a flat band, therefore confirming the existence of OTI.

In Chapter 5, we examine the tunability of edge states of 2D organometallic frameworks by using a different metal atom and molecular ligand than those of the lattice studied in Chapter 4. The recent theoretically predicted topological states and flat Chern band (FCB) in 2D organometallic frameworks could penetrate several areas in condensed matter physics, organic chemistry, and materials science. The high tunability of such 2D frameworks by using different metal atoms and molecular ligands could greatly expand the family of topological materials and significantly ease the process of designing of such materials with specific properties. Here, we proposed a design of a 2D organometallic lattice, consisting of π-conjugated thallium ions and benzene ring with a chemical formula Tl_2Ph_3, which exhibits nontrivial topological states with a large gap in both a nearly flat band around the Fermi level and a Dirac band. We note that the Tl_2Ph_3 lattice has the largest spin orbit coupling (SOC) gap among all the theoretically proposed organic topological insulators so

far.

1.5 Reference

[1] K. S. Novoselov, A. K. Geim, S. V. Morozov, D. Jiang, Y. Zhang, S. V. Dubonos, I. V. Grigorieva, and A. A. Firsov, Science **306**, 666 (2004).

[2] K. S. Novoselov, D. Jiang, F. Schedin, T. J. Booth, V. V. Khotkevich, S. V. Morozov, and A. K. Geim, Proc. Natl. Acad. Sci. U. S. A. **102**, 10451 (2005).

[3] A. Fasolino, J. Los, and M. I. Katsnelson, Nat. Mater. **6**, 858 (2007).

[4] J. C. Meyer, A. K. Geim, M. Katsnelson, K. Novoselov, T. Booth, and S. Roth, Nature (London) **446**, 60 (2007).

[5] L. Landau, Phys. Z. Sowjetunion **11**, 26 (1937).

[6] N. D. Mermin, Phys. Rev. **176**, 250 (1968).

[7] N. D. Mermin and H. Wagner, Phys. Rev. Lett. **17**, 1133 (1966).

[8] C. Lee, X. Wei, J. W. Kysar, and J. Hone, Science **321**, 385 (2008).

[9] A. K. Geim and K. S. Novoselov, Nat. Mater. **6**, 183 (2007).

[10] Y. Zhang, Y.-W. Tan, H. L. Stormer, and P. Kim, Nature (London) **438**, 201 (2005).

[11] A. A. Balandin, S. Ghosh, W. Bao, I. Calizo, D. Teweldebrhan, F. Miao, and C. N. Lau, Nano Lett. **8**, 902 (2008).

[12] I. Meric, M. Y. Han, A. F. Young, B. Ozyilmaz, P. Kim, and K. L. Shepard, Nat. Nanotechnol. **3**, 654 (2008).

[13] C. L. Kane and E. J. Mele, Phys. Rev. Lett. **95**, 146802 (2005).

[14] C. L. Kane and E. J. Mele, Phys. Rev. Lett. **95**, 226801 (2005).

[15] J. C. Boettger and S. B. Trickey, Phys. Rev. B **75**, 121402 (2007).

[16] M. Gmitra, S. Konschuh, C. Ertler, C. Ambrosch-Draxl, and J. Fabian, Phys. Rev. B **80**, 235431 (2009).

[17] D. Huertas-Hernando, F. Guinea, and A. Brataas, Phys. Rev. B **74**, 155426 (2006).

[18] H. Min, J. E. Hill, N. A. Sinitsyn, B. R. Sahu, L. Kleinman, and A. H. MacDonald, Phys. Rev. B **74**, 165310 (2006).

[19] Y. Yao, F. Ye, X.-L. Qi, S.-C. Zhang, and Z. Fang, Phys. Rev. B **75**, 041401 (2007).

[20] Z. Liu, Z.-F. Wang, J.-W. Mei, Y.-S. Wu, and F. Liu, Phys. Rev. Lett. **110**, 106804 (2013).

[21] Z. Wang, Z. Liu, and F. Liu, Nat. Commun. **4**, 1471 (2013).

[22] Z. F. Wang, Z. Liu, and F. Liu, Phys. Rev. Lett. **110**, 196801 (2013).

[23] A. K. Geim, Rev. Mod. Phys. **83**, 851 (2011).

[24] M. Z. Hasan and C. L. Kane, Rev. Mod. Phys. **82**, 3045 (2010).

[25] K. S. Novoselov, Rev. Mod. Phys. **83**, 837 (2011).

[26] X.-L. Qi and S.-C. Zhang, Rev. Mod. Phys. **83**, 1057 (2011).

[27] E.-A. Kim and A. H. C. Neto, Europhys. Lett. **84**, 57007 (2008).

[28] V. M. Pereira and A. H. Castro Neto, Phys. Rev. Lett. **103**, 046801 (2009).

[29] V. M. Pereira, A. H. Castro Neto, and N. M. R. Peres, Phys. Rev. B **80**, 045401 (2009).

[30] S. S. Datta, D. R. Strachan, S. M. Khamis, and A. T. C. Johnson, Nano Lett. **8**, 1912 (2008).

[31] . . Girit, J. C. Meyer, R. Erni, M. D. Rossell, C. Kisielowski, L. Yang, C.-H. Park, M. F. Crommie, M. L. Cohen, S. G. Louie, and A. Zettl, Science **323**, 1705 (2009).

[32] X. Jia, M. Hofmann, V. Meunier, B. G. Sumpter, J. Campos-Delgado, J. M. Romo-Herrera, H. Son, Y.-P. Hsieh, A. Reina, J. Kong, M. Terrones, and M. S. Dresselhaus, Science **323**, 1701 (2009).

[33] Y. Lu, B. Goldsmith, D. R. Strachan, J. H. Lim, Z. Luo, and A. T. C. Johnson, Small **6**, 2748 (2010).

[34] Q. Yan, B. Huang, J. Yu, F. Zheng, J. Zang, J. Wu, B.-L. Gu, F. Liu, and W. Duan, Nano Lett. **7**, 1469 (2007).

[35] W. J. Yu, S. H. Chae, D. Perello, S. Y. Lee, G. H. Han, M. Yun, and Y. H. Lee, ACS Nano **4**, 5480 (2010).

[36] M. H. Gass, U. Bangert, A. L. Bleloch, P. Wang, R. R. Nair, and A. Geim, Nat. Nanotechnol. **3**, 676 (2008).

[37] J. Y. Huang, F. Ding, B. I. Yakobson, P. Lu, L. Qi, and J. Li, Proc. Natl. Acad. Sci. U. S. A. **106**, 10103 (2009).

[38] Z. Liu, K. Suenaga, P. J. F. Harris, and S. Iijima, Phys. Rev. Lett. **102**, 015501 (2009).

[39] A. Cresti, M. M. Fogler, F. Guinea, A. H. Castro Neto, and S. Roche, Phys. Rev. Lett. **108**, 166602 (2012).

[40] S. Cranford, D. Sen, and M. J. Buehler, Appl. Phys. Lett. **95**, (2009).

[41] J. S. Bunch, S. S. Verbridge, J. S. Alden, A. M. van der Zande, J. M. Parpia, H. G. Craighead, and P. L. McEuen, Nano Lett. **8**, 2458 (2008).

[42] J. S. Bunch, A. M. van der Zande, S. S. Verbridge, I. W. Frank, D. M. Tanenbaum, J. M. Parpia, H. G. Craighead, and P. L. McEuen, Science **315**, 490 (2007).

[43] K. S. Kim, Y. Zhao, H. Jang, S. Y. Lee, J. M. Kim, K. S. Kim, J.-H. Ahn, P. Kim, J.-Y. Choi, and B. H. Hong, Nature (London) **457**, 706 (2009).

[44] T. M. G. Mohiuddin, A. Lombardo, R. R. Nair, A. Bonetti, G. Savini, R. Jalil, N. Bonini, D. M. Basko, C. Galiotis, N. Marzari, K. S. Novoselov, A. K. Geim, and A. C. Ferrari, Phys. Rev. B **79**, 205433 (2009).

[45] Z. H. Ni, T. Yu, Y. H. Lu, Y. Y. Wang, Y. P. Feng, and Z. X. Shen, ACS Nano **2**, 2301 (2008).

[46] G. Tsoukleri, J. Parthenios, K. Papagelis, R. Jalil, A. C. Ferrari, A. K. Geim, K. S. Novoselov, and C. Galiotis, Small **5**, 2397 (2009).

[47] W. Bao, F. Miao, Z. Chen, H. Zhang, W. Jang, C. Dames, and C. N. Lau, Nat. Nanotechnol. **4**, 562 (2009).

[48] F. Guinea, M. Katsnelson, and A. Geim, Nat. Phys. **6**, 30 (2010).

[49] F. de Juan, A. Cortijo, M. A. Vozmediano, and A. Cano, Nat. Phys. **7**, 810 (2011).

[50] N. Levy, S. A. Burke, K. L. Meaker, M. Panlasigui, A. Zettl, F. Guinea, A. H. C. Neto, and M. F. Crommie, Science **329**, 544 (2010).

[51] V. Shenoy, C. Reddy, A. Ramasubramaniam, and Y. Zhang, Phys. Rev. Lett. **101**, 245501 (2008).

[52] E. Prada, P. San-Jose, G. Len, M. M. Fogler, and F. Guinea, Phys. Rev. B **81**, 161402 (2010).

[53] Y. Zhang and F. Liu, Appl. Phys. Lett. **99**, (2011).

[54] K. v. Klitzing, G. Dorda, and M. Pepper, Phys. Rev. Lett. **45**, 494 (1980).

[55] D. J. Thouless, M. Kohmoto, M. P. Nightingale, and M. den Nijs, Phys. Rev. Lett. **49**, 405 (1982).

[56] M. V. Berry, Proc. R. Soc. London, Ser. A **392**, 45 (1984).

[57] F. Haldane, Phys. Rev. Lett. **61**, 2015 (1988).

[58] D. N. Sheng, Z. Y. Weng, L. Sheng, and F. D. M. Haldane, Phys. Rev. Lett. **97**, 036808 (2006).

[59] Z. Wang, N. Su, and F. Liu, Nano Lett. **13**, 2842 (2013).

[60] T. Kambe, R. Sakamoto, K. Hoshiko, K. Takada, M. Miyachi, J.-H. Ryu, S. Sasaki, J. Kim, K. Nakazato, M. Takata, and H. Nishihara, J. Am. Chem. Soc. **135**, 2462 (2013).

CHAPTER 2

CHEMICAL VERSUS THERMAL FOLDING OF GRAPHENE EDGES

2.1 Introduction

Graphene has attracted much recent interest due to its fascinating physical and chemical properties [1].One fundamental question for graphene is its thermal and chemical stability, since this has important implications for its practical applications. As an ultrathin two-dimensional structure only one-atomic-layer thick, graphene can undergo large out-of-plane thermal fluctuations [2]. The presence of free edges makes the graphene susceptible to edge defects and chemical impurities [3] as well as to mechanical edge warping and twisting instability [4-6]. Furthermore, several recent experiments [7-10] have observed folded graphene edges, which raises several interesting questions: (1) Are the folded edges an intrinsic or extrinsic property of graphene edge stability? (2) What is the kinetic energy barrier associated with the folding process? (3) How does the folding process depend on the chemical environment? Our aim here is to answer these fundamental questions by comparing the thermal and chemical folding processes at graphene edges, using molecular simulations. It is worth pointing out that understanding the graphene edge folding process is not only of scientific interest, but also of technological importance. For example, one very recent experiment has shown that the transport properties of open and closed graphene edges are very different, with the closed edge exhibiting a much higher conductivity [11].

A suspended free-standing graphene edge has been observed by transmission electron microscopy (TEM) to fold over [7, 8], forming a structure similar to one-half of a single-walled carbon nanotube (SWCNT). Using high resolution TEM, Liu et al. [9] have further shown that both armchair and zigzag edges of graphene exhibit a folded edge state. Moreover, *in situ* observation of multilayer graphene has demonstrated that both the armchair and zigzag edges can form folded structures spontaneously at about 2400 K [10]. On the other hand, a theoretical study using a coarse-grained hierarchical multiscale model has shown that the

folded edges are thermodynamically stable beyond a critical folded length [12], and a kinetic Monte Carlo calculation was consistent with the observed spontaneous folding process at high temperature (∼2400 K) [10]. Recently, quantum molecular dynamics simulations also uncovered the roles of edge reconstruction, carbon vacancies, and interstitials in the thermal folding process of double-layer graphene (DLG) at high temperature (1000 K), which explained why the closed edge structure forms under Joule heating only if the sample is not irradiated by high-energy electrons [13]. Another simulation studied folding of a Y-shape graphene ribbon at high temperature [14].

Although previous theoretical studies [10, 12, 13] have confirmed folding of single-layer graphene (SLG) and DLG edges at high temperatures, the kinetics associated with the graphene edge folding process, which determine the feasibility of edge folding at different temperatures (including room temperature) and in different chemical environments, remains unexplored. Most importantly, the energy barriers associated with the folding processes of both SLG and DLG edges remain unknown. We noticed that the graphene preparation methods used in Refs. [7-9] all involved initial working in solution without subsequent purification steps. For example, the graphene membranes prepared by Meyer et al. [7] were treated in water, isopropanol, acetone, and liquid carbon dioxide, while Liu et al. [9] used heat treatment of graphite powder dispersed in ethanol by ultrasonication before dropping the resulting graphene onto a grid. Thus, these graphene membranes may be polluted by adsorbates, which may chemically assist the graphene edge folding processes [14]. Therefore, besides thermal folding of clean graphene edges, i.e., a thermally activated process, chemical folding of graphene edges with adsorbates, i.e., a chemisorption-assisted process should be considered. In particular, we must determine the energy barriers for thermal versus chemical folding of graphene edges, to assess the feasibility of graphene edge folding processes at different temperatures and in different chemical environments.

2.2 Methodology

We have carried out extensive molecular dynamics simulations to derive the limiting kinetic energy barriers for edge folding processes of both SLG and DLG, using a modified form of the bond-order potential due to Brenner et al. [15] and a similar setup as before [14]. Our own Lennard-Jones (L-J) potential parameters [14] were developed to give a ∼42 meV/atom interlayer cohesive energy for graphite, in accordance with experiment [16]. We studied H adsorption as a simple model system for chemical folding, using a new bond-order term for C-H to give a H adsorption energy of ∼0.9 eV on graphite, as predicted

by first-principles calculations [14]. (The original Brenner potential predicted a H adsorption energy about 1.7 eV higher.) For all the MD simulations, periodic boundary conditions were only employed in the direction along the edge. The simulations were performed at $T = 150$ K in order to suppress thermal fluctuations. We note that because the edge folding energy barrier comes mainly from bending energy, involving no chemical bond breaking/formation energy, it can be well described by a classical potential. Thus, we opted to use a classical potential instead of a first-principles method to derive the folding energy barrier in order to save computational time. In the unfolding process, there will be bond breaking associated with van der Waals interlayer interactions. So one may expect our calculated unfolding barriers to be less accurate than the calculated folding barriers, but this will not affect our conclusions on edge folding feasibility, which is solely determined by the folding barriers.

2.3 Thermodynamic Driving Force for Edge Folding

Before exploring the kinetics associated with the graphene edge folding process, we first study the thermodynamic driving force for edge folding because the folded edge structure can be more stable than the flat edges. Figure 2-1 illustrates the energy minimization simulations to show the stability of the folded graphene edge. We generate an edge-folded SLG sheet with an overlapping length l and folding length L, as shown in Figure 2-1a. Then, we release the folded edge by moving the upper portion toward the right along the $+x$-direction to reduce l in steps of 1 Å (from Figure 2-1a1 to Figure 2-1a3), and the potential energy is calculated at each step, as shown in Figure 2-1b. The folded edge energy per edge length relative to the unfolded edge is

$$E_e = \gamma_i \times l + \gamma_b \tag{2.1}$$

where γ_i and γ_b are the interlayer van der Waals (vdW) bonding energy of the overlapping portion and the bending energy of the folding portion, respectively. γ_b is a constant because the shape of the folding portion remains the same with almost constant $L = 22$ Å, as l is reduced (see Figures 2-1a1-3). In calculating the potential energy as a function of l in Figure 2-1b, the energy of the flat SLG is set as the zero point of the energy (shown in Figure 2-1b as a black dashed line).

The data show a nice linear relation as expected, and the interlayer bonding energy obtained from the linear fitting (the slope of the red solid line in Figure 2-1b) gives $\gamma_i \approx 15$ meV/Å^2, or about 42 meV/atom, consistent with the L-J potential used. The E_e value at $l = 0$ gives the bending energy $\gamma_b \approx 306$ meV/Å, or about 625 meV/atom. By extrapolation,

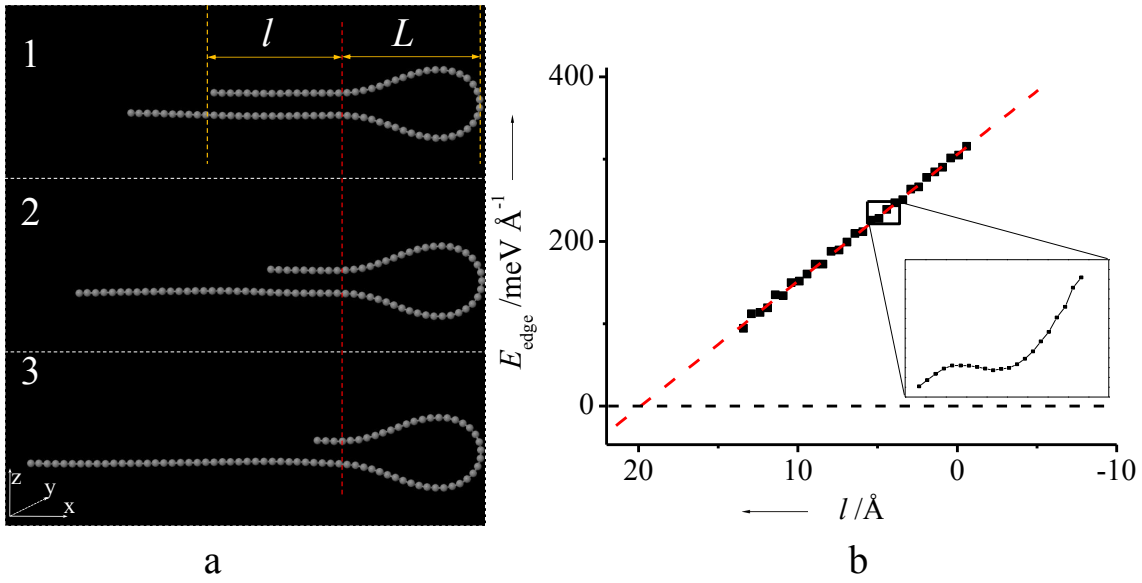

Figure 2.1. Energy minimization simulation of the edge-folded SLG. (a) Structures of the edge-folded SLG with different lengths of overlap portion. L and l are overlapping length and folding length, respectively. The grey balls are carbon atoms. The red dashed line represents the reference plane for measuring l and L. (b) The folded edge energy as a function of folding length. Dotted line: energy of flat graphene (set to be zero). Solid line: linear fit to the data (solid black squares). The inset shows the fine structure of the E-l curve.

the folded edge of the SLG is seen to be more stable than the flat edge if $l > 20$ Å, when the energy gain from the interlayer vdW bonding of the overlapping portion overcomes the energy cost from the bending of the folding portion. In addition, the potential energy is microscopically affected by the atomic stacking of the overlapping portion, which leads to a periodic fluctuation of the $E_e - l$ curve, as shown in the inset of Figure 2-1b.

2.4 Kinetic Barriers for Thermal Folding

Even though the folded edge structure can be thermodynamically more stable than the flat edge, the folding process may still be prohibited by a large kinetic barrier, especially for a thermally activated process. Next, we derive the energy barriers for the edge folding processes. We note that we do not attempt to directly simulate the folding process of a graphene edge, because the process is too complex and requires much too long a simulation time. So, instead, we will use MD simulation as an effective method to derive the limiting kinetic barriers for edge folding. We consider that the folding starts locally at one place then spreads around the whole edge (like a zipping effect). The initial local folding is thus the rate-limiting step and the barrier, which should be defined by energy per length, largely determines the overall folding probability because the remaining edges have much smaller barriers per length. However, it is very difficult (if not impossible) to determine this rate-limiting barrier because it may not have a unique value, but rather depend on how the folding process actually occurs and change with edge length. On the other hand, we can establish the lower-bound of this barrier by assuming the edge folds collectively, or in other words, as soon as the initial folding starts somewhere, the remaining edges follow immediately, as we have done here.

For convenience, the unfolding process of SLG, which is the reverse process of folding, is simulated in order to obtain the energy barrier of folding as shown in Figure 2-2. First, the atomic positions in a folded SLG edge are relaxed for 30 ps (Figure 2-2a1). Then, a horizontal force is applied (the force is applied every 30 ps and sustained for 0.2 ps periodically) on all the carbon atoms in the upper portion (both the overlapping and folding portions) of the folded edge along the $+x$-direction. The long simulation time of ~30 ps is used to make sure that local equilibration is reached each time after the force is applied, so as to obtain the lowest energy configuration at a given folding position (i.e., the degree of fold), and hence to guarantee that the lowest barrier is obtained, in the unfolding process as well as in the folding process.

The energy per edge atom as a function of time during the unfolding process is shown

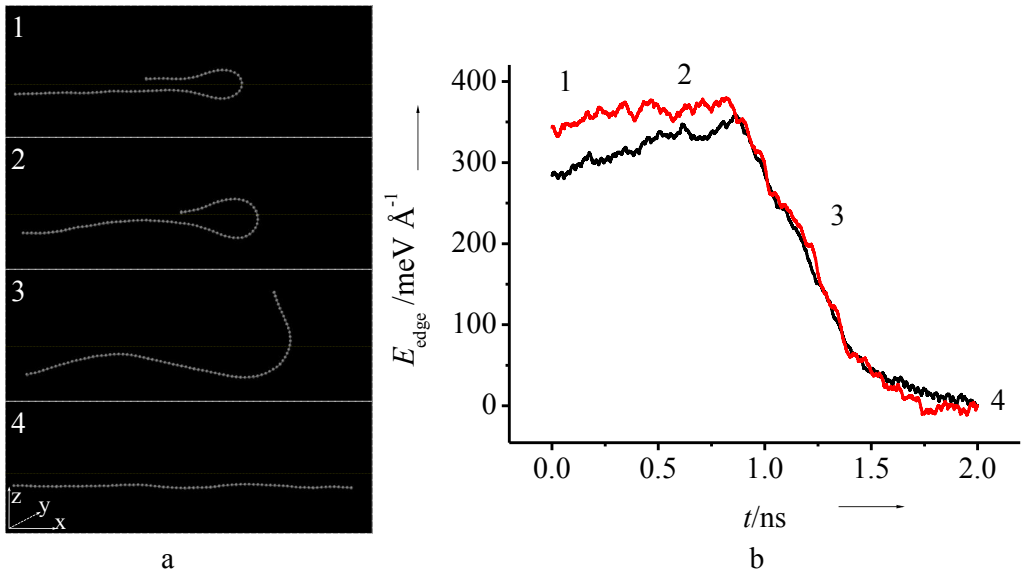

Figure 2.2. Unfolding process of SLG. (a) Structures of SLG during classical molecular dynamics simulation of the unfolding process (from 1 to 4). (b) The folded edge energy as a function of time during the unfolding process (black and red solid lines represent armchair and zigzag edges, respectively). The energy of the flat SLG is set to be zero.

in Figure 2-2b. Initially, E_e increases due to a decrease in the interlayer bonding vdW energy by virtue of the reduction in the area of the overlapping portion, and subsequently decreases due to the decrease in bending energy associated with unfolding the folding portion. Finally, the SLG sheet becomes flat (Figure 2-2a3). The energy barriers for edge folding of the SLG (in reference to the flat edge, Figure 2-2a4) are approximately 360 meV/Å (or 780 meV/atom) and 380 meV/Å (or 830 meV/atom) for armchair and zigzag edges, respectively; these values are about 30 times larger than the thermal energy per atom at room temperature (RT, ~26 meV/atom).

The folded-edge structure can also be obtained by bonding of the top and bottom edges of the DLG (Figure 2-3). In this case, both edges undergo a much smaller bending to form the folded edge than in the SLG folding process, and hence the energy barrier is expected to be lower. To obtain the energy barrier, a DLG with open edges is first relaxed for 30 ps (Figure 2-3a1); periodic forces of opposite directions are then applied vertically on the edge atoms along the z-direction to push them toward each other (Figure 2-3a2) to form the closed-edge structure (Figure 2-3a3). The change in potential energy is calculated and shown in Figure 2-3b. The energy barriers for DLG to form the closed edge structures are about 55 meV/Å (or 120 meV/atom) for both armchair and zigzag edges.

Given the energy barrier, according to transition-state theory, the possibility of edge folding P follows

$$P \approx \nu e^{-E_b/k_B T} \tag{2.2}$$

where E_b, k_B , ν, and T are the energy barrier, Boltzmann constant, attempt frequency, and temperature, respectively. ν is related to the vibrational frequency of edge atoms. Since the edge atoms have to vibrate in a collective manner in order to fold, the attempt frequency is expected to be much smaller than the single atom vibration frequency (the typical order of the atomic vibration frequency is $\sim 10^{13}$ s^{-1}). At RT, the $e^{-E_b/k_B T}$ factor is about $\sim 10^{-14}$ for the folding of SLG, and $\sim 10^{-2}$ for the folding of DLG. Consequently, at RT the probability of thermal edge folding of both SLG and DLG is very small. But at high temperatures, thermal folding of DLG is feasible. This is consistent with the experiments of Huang et al. who observed spontaneous edge folding of DLG at $k_B T \approx 200$ meV [10] and quantum molecular dynamics results at $k_B T \approx 90$ meV [13].

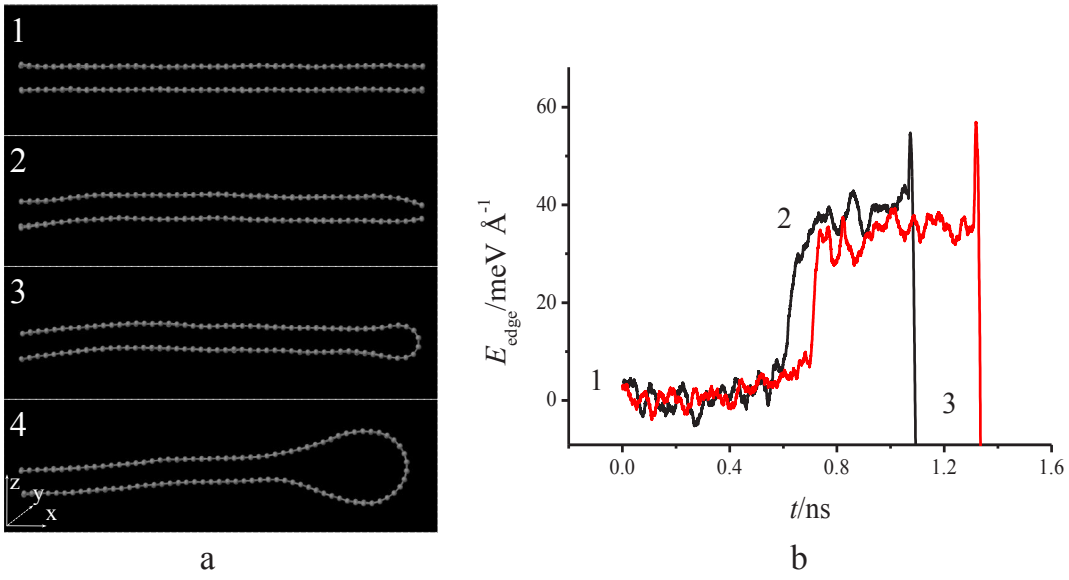

Figure 2.3. Folding process of DLG. (a) Structures of DLG during classical molecular dynamics simulation of the folding process (from 1 to 4). (b) The folded edge energy as a function of time during the folding process (black and red solid lines represent armchair and zigzag edges, respectively). The energy of the flat DLG is set to be zero.

2.5 Kinetic Barriers for Chemical Folding

Next, we explore the chemisorption-assisted edge folding process (chemical folding) since, as discussed above, atomic and molecular adsorbates are probably involved in the experimental folding process. It has been shown that chemisorption of H atoms leads to a change in the hybridization of the carbon atom where H is adsorbed from sp^2 to sp^3 [14]. If H atoms are adsorbed only on one side of graphene (or on both sides with different coverage), then they will introduce a tensile stress in the graphene sheet providing a driving force for rolling up the edge of graphene [14]. Assuming one-side adsorption, the stress increases with H coverage and goes up to 800 meV/Å^2 [14] at the experimental upper limit of H coverage on a graphite surface [17]. Recent experiments have also achieved scrolling up of flat graphene by atom/molecule adsorption [18, 19]. To test the feasibility of chemical folding of graphene edges, for simplicity, we use H atoms adsorbed on one side of graphene in order to explore the effect of adsorbates. We first derived the energy barrier as a function of H coverage (Figure 2-4), from the energy curves like those in Figures 2-2 and 2-3 for the process without H (the $E_e - l$ curve for the SLG edge folding at 5% H coverage is shown in Figure 2-5 as an example). Our results show that the energy barrier of folding decreases significantly as H coverage increases. At ∼14% H coverage, the energy barrier vanishes, which means that the edge of SLG can fold spontaneously at this H coverage or higher.

Furthermore, we performed MD simulations to directly observe the chemical folding process. First, a sheet of SLG without adsorbate is relaxed for 30 picoseconds. Then hydrogen atoms at ∼50% coverage [20] are absorbed on the bottom side of suspended graphene with a random distribution. Driven by the stress induced by hydrogen adsorption, the edge begins to bend up and finally forms the folded structure.

Similarly, a DLG is relaxed for 30 picoseconds, and then 30% H coverage [20] is introduced at the near-edge region of both layers. The edge of the upper layer bends down while the edge of the bottom layer bends up and they meet and bond together to form a closed structure. Finally, the curved portion expands to release strain energy until $\partial E_{strain}/\partial L = -\partial E_{vdW}/\partial L$, where E_{strain} and E_{vdW} are the bending strain energy and the interfacial vdW bonding energy, respectively (a movie showing this process is available in the ESM). These results demonstrate that the edge of graphene may fold spontaneously with sufficiently high one-side (or imbalanced two-side [21]) hydrogen adsorption at room temperature, indicating a spontaneous chemical folding process. It is interesting to see that chemical adsorption of H promotes the edge folding of DLG, while in contrast, vacancies and impurities inhibit the edge folding of DLG [13].

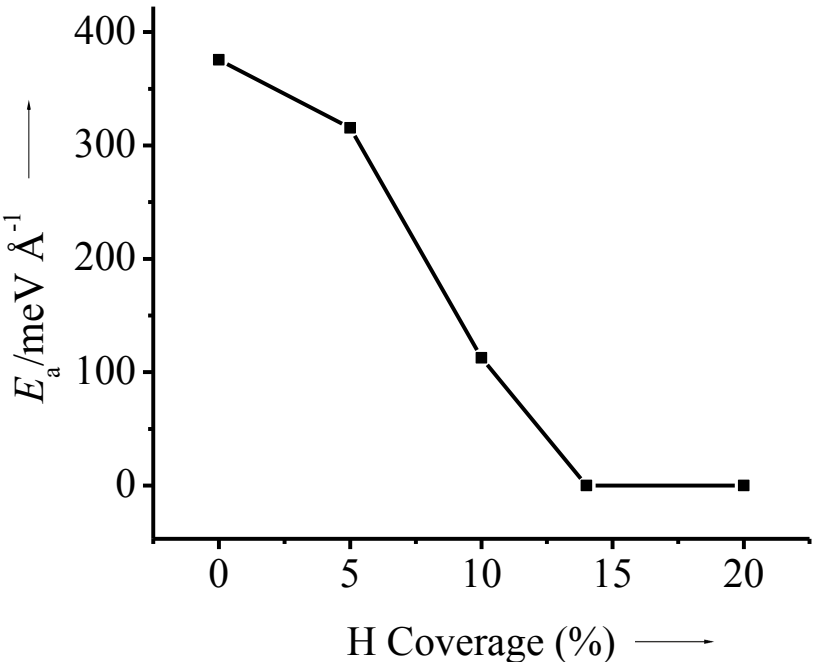

Figure 2.4. The energy barrier for SLG edge folding as a function of H coverage.

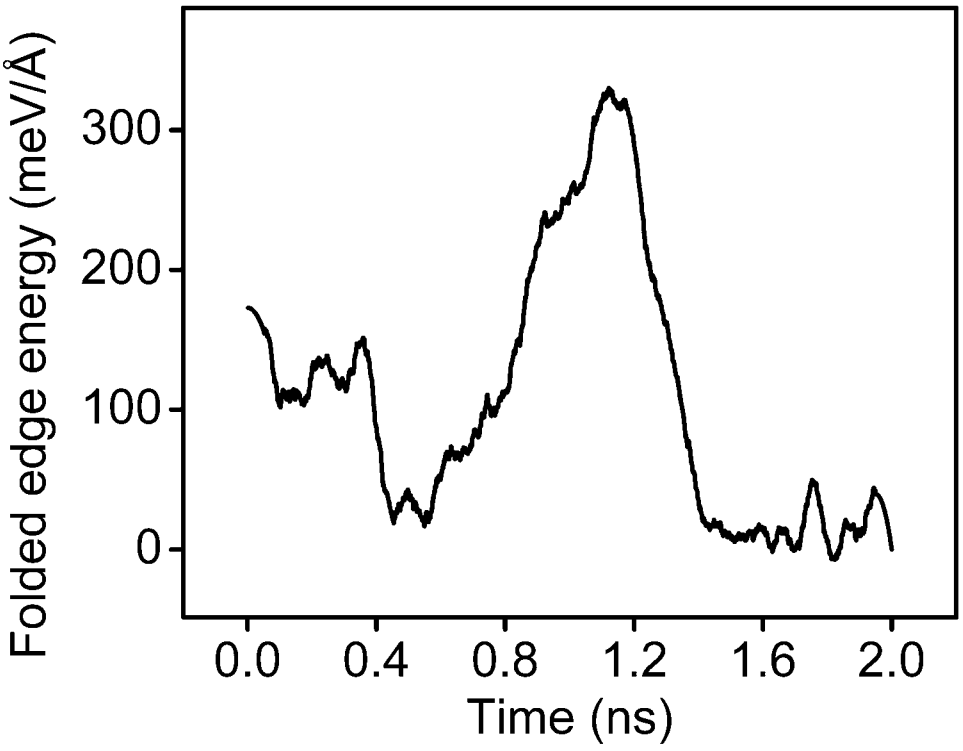

Figure 2.5. The energy barrier for SLG edge folding at 5% H coverage.

Although we have only studied H adsorption here, other adsorbates may have the same effect. One basic condition is for the adsorbates to induce a tensile surface stress and fold the graphene by converting the C bonding configuration from sp^2 to sp^3. One example is F, which has previously been shown to fold graphene nanoribbons into nanotubes [14]. We also note that if graphene is on a substrate other than graphite, our approach will work best with a very weak interaction between graphene and the substrate, such as the van der Waals type of interaction found for graphite itself.

2.6 Conclusion

In conclusion, we have derived for the first time the kinetic energy barriers for bending of SLG and DLG edges to form a closed edge structure. Based on the energy barriers, we conclude that thermal edge folding of SLG is generally not feasible, while thermal edge folding of DLG is feasible at high temperature but not at room temperature. However, edge folding barriers can be greatly reduced by imbalanced chemisorption of atoms or molecules (as demonstrated for H) on the two sides of graphene, which may even lead to spontaneous edge folding of both SLG and DLG at room temperature. Our findings indicate that the formation of suspended graphene with folded edges as observed in some experiments at room temperature [7-9] may involve assistance by adsorbates.

2.7 Reference

[1] Q. Yan, B. Huang, J. Yu, F. Zheng, J. Zang, J. Wu, B.-L. Gu, F. Liu, and W. Duan, Nano Lett. **7**, 1469 (2007).

[2] A. Fasolino, J. Los, and M. I. Katsnelson, Nat. Mater. **6**, 858 (2007).

[3] B. Huang, F. Liu, J. Wu, B.-L. Gu, and W. Duan, Phys. Rev. B **77**, 153411 (2008).

[4] V. Shenoy, C. Reddy, A. Ramasubramaniam, and Y. Zhang, Phys. Rev. Lett. **101**, 245501 (2008).

[5] K. Bets and B. Yakobson, Nano Res. 2, 161 (2009).

[6] B. Huang, M. Liu, N. Su, J. Wu, W. Duan, B. Gu, and F. Liu, Phys. Rev. Lett. **102**, 166404 (2009).

[7] J. C. Meyer, A. K. Geim, M. Katsnelson, K. Novoselov, T. Booth, and S. Roth, Nature (London) **446**, 60 (2007).

[8] M. H. Gass, U. Bangert, A. L. Bleloch, P. Wang, R. R. Nair, and A. Geim, Nat. Nanotechnol. **3**, 676 (2008).

[9] Z. Liu, K. Suenaga, P. J. F. Harris, and S. Iijima, Phys. Rev. Lett. **102**, 015501 (2009).

[10] J. Y. Huang, F. Ding, B. I. Yakobson, P. Lu, L. Qi, and J. Li, Proc. Natl. Acad. Sci. U. S. A. **106**, 10103 (2009).

[11] W. J. Yu, S. H. Chae, D. Perello, S. Y. Lee, G. H. Han, M. Yun, and Y. H. Lee, ACS Nano **4**, 5480 (2010).

[12] S. Cranford, D. Sen, and M. J. Buehler, Appl. Phys. Lett. **95**, (2009).

[13] E. Cruz-Silva, A. R. Botello-Mndez, Z. M. Barnett, X. Jia, M. S. Dresselhaus, H. Terrones, M. Terrones, B. G. Sumpter, and V. Meunier, Phys. Rev. Lett. **105**, 045501 (2010).

[14] D. Yu and F. Liu, Nano Lett. **7**, 3046 (2007).

[15] D. W. Brenner, O. A. Shenderova, J. A. Harrison, S. J. Stuart, B. Ni, and S. B. Sinnott, J. Phys.: Condens. Matter **14**, 783 (2002).

[16] L. A. Girifalco and R. A. Lad, J. Chem. Phys. **25**, 693 (1956).

[17] T. Zecho, A. Guttler, X. Sha, B. Jackson, and J. Kuppers, J. Chem. Phys. **117**, 8486 (2002).

[18] X. Xie, L. Ju, X. Feng, Y. Sun, R. Zhou, K. Liu, S. Fan, Q. Li, and K. Jiang, Nano Lett. **9**, 2565 (2009).

[19] A. Sidorov, D. Mudd, G. Sumanasekera, P. J. Ouseph, C. S. Jayanthi, and S.-Y. Wu, Nanotechnology **20**, 055611 (2009).

CHAPTER 3

QUANTUM MANIFESTATIONS OF GRAPHENE EDGE STRESS AND EDGE INSTABILITY: A FIRST-PRINCIPLES STUDY

3.1 Introduction

Graphene, a two-dimensional (2D) single layer of carbon atoms, has exhibited unique electronic properties [1] and potential applications in electronic devices [2]. Earlier studies have focused on characterizing the unusual electronic and transport properties of graphene, particularly as a massless Dirac fermion system [1,2]. Some recent attention has been shifted to the structural stability of graphene [2-5]. On one hand, as a 2D membrane structure, graphene provides an ideal testing ground [3,4] for the classical Mermin-Wagner theorem on the existence of long-range crystalline order in 2D [6,7]. On the other hand, the free edges of graphene are amenable to edge instabilities [5,8-10]. The graphene edge stability is defined by two fundamental thermodynamic quantities: edge energy and edge stress. The edge of a 2D structure can be understood in analogy to the surface of a 3D structure [11,12]: the edge (surface) energy accounting for the energy cost to create an edge (surface) defines the edge (surface) chemical stability; the edge (surface) stress accounting for the energy cost to deform an edge (surface) defines the edge (surface) mechanical stability. First-principles calculations showed that chemically, the armchair edge is more stable with a lower energy, while the zigzag edge is metastable against reconstruction [8]. Empirical-potential calculations showed that both intrinsic edges are under compressive stress, rendering a mechanical edge twisting and warping instability [10].

Usually, stress and mechanical instability are understood as phenomena of classical mechanics, but they are expected to be affected by quantum effects which become prominent at nanoscale. So far, however, quantum effects have been mostly shown for electronic

structure and energetic quantities of low-dimensional nanostructures. Here, we demonstrate an interesting example of quantum manifestations of mechanical quantities in graphene edge stress. Using first-principles calculations, we predict that the armchair edge stress in a nanoribbon exhibits a large oscillation with ribbon width arising from quantum size effect, while the zigzag edge stress is reduced by spin polarization. Such quantum effects on edge stress in turn manifest in graphene edge mechanical instability, with "quantum" features that apparently cannot be described by empirical potentials or continuum theory.

3.2 Intrinsic Edge Stress of Graphene

Our calculations were performed using the density functional theory (DFT) method as implemented in the VASP code [13]. The supercell technique was adopted to model the graphene nanoribbons (GNR), with a vacuum layer > 15Å. We used a plane-wave energy cutoff of 500 eV and optimized structure until the atomic forces converged to $< 10meV/$Å. The edge energy is calculated as $E_{edge} = (E_{ribbon} - E_{atom})/2L$, where E_{ribbon} is the total energy of the graphene nanoribbon, E_{atom} is the energy per atom in a perfect graphene, and L is the length of edge. The edge stress is calculated as $\sigma_{edge} = \sigma_{xx}/2$, where σ_{xx} is the diagonal component of supercell stress tensor in the x-direction (defined along the edge), which is calculated using the Nielsen-Martin algorithm [14]. All other components of stress tensor vanish. We note that DFT is suitable for calculating ground-state properties of lattice energies and stresses, to which the nonlocal many-body effects are not important.

Figure 3.1 shows the edge energy and edge stress of armchair edges as a function of ribbon width from ∼3.5 to 48Å. One notices that both edge energy and edge stress oscillate with the increasing width having a period of 3 but out of phase with each other. The oscillations are originated from the quantum confinement effect, as seen in the similar oscillations of electron band structures [15-18]. The oscillation of edge energy decays quickly with the increasing width and converges to ∼1.0 eV/Å, which agrees well with the previous first-principles values [8]. In contrast, the oscillation of edge stress decays much slower with a mean value of ~ -1.45 eV/Å (using a negative sign as the convention for compressive stress). The much larger oscillation in edge stress than in edge energy is possibly caused by the fact that edge stress equals to the derivative of edge energy with respect to strain so that stress is much more sensitive to the width-dependent quantum confinement effect. There is also a slight revival effect in the stress oscillations at ∼40Å width, whose origin is not clear and needs further study.

Figure 3.2 shows the edge energy and edge stress of GNR zigzag edges as a function of

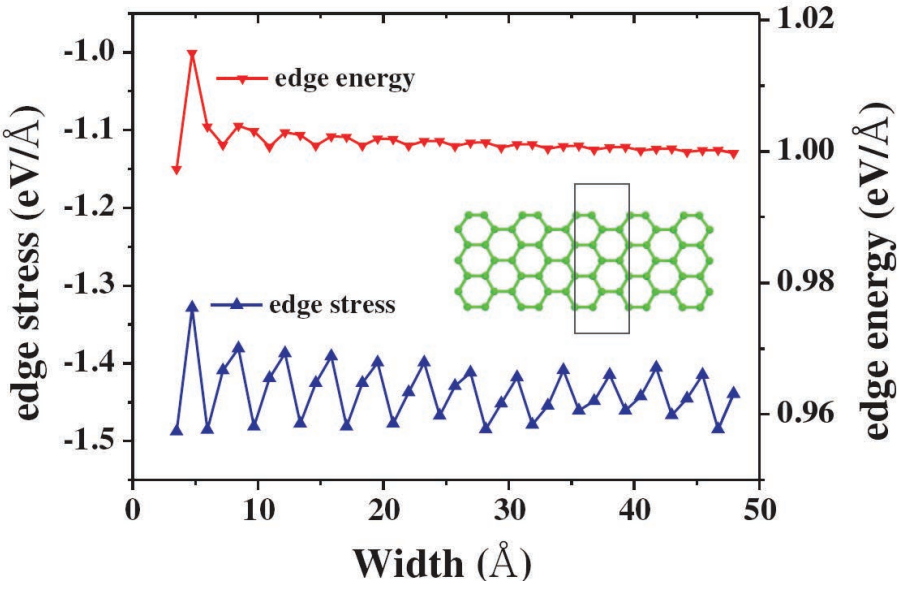

Figure 3.1. The armchair edge stresses and edge energies of graphene nanoribbons as a function of ribbon width. Inset: schematics of the nanoribbon; the rectangle marks one unit cell (supercell) of the ribbon.

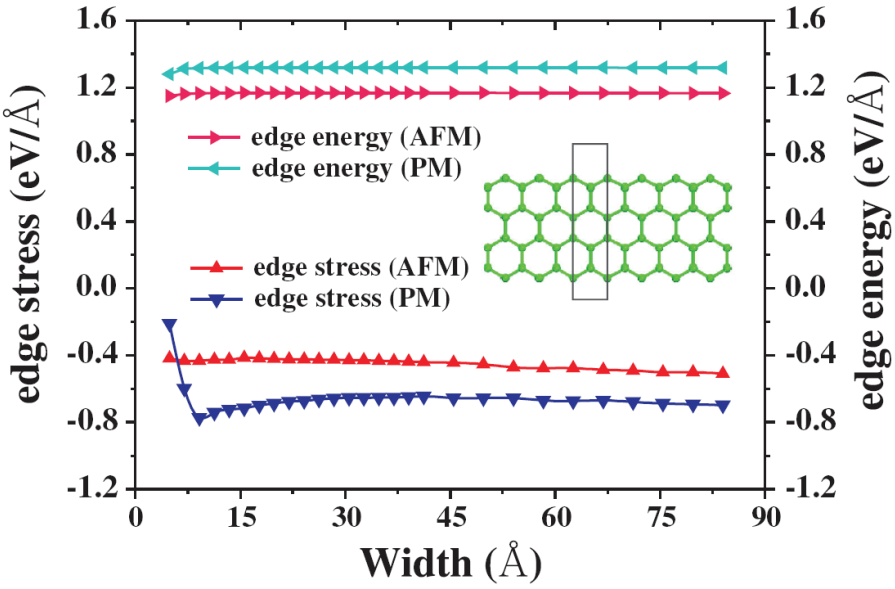

Figure 3.2. The AFM and PM zigzag edge stresses and edge energies of graphene nanoribbons as a function of ribbon width. Inset: schematics of the nanoribbon; the rectangle marks one unit cell (supercell) of the ribbon.

ribbon width from ∼5.0 to 85 Å. In this case, both edge energy and edge stress show very weak width dependence and converges quickly, again consistent with their corresponding electronic-structure behavior [15-18]. However, the zigzag edge is known to have an antiferromagnetic (AFM) ground state [17]. The AFM edge energy is calculated to be ∼1.2 eV/Å, about 0.2 eV/Å lower than the paramagnetic (PM) edge energy [8,9,19]. Thus, we have calculated the spin dependence of edge stress and found that spin polarization reduces the compressive stress from ~ -0.7 eV/Å in the PM edge to ~ -0.5 eV/Å in the AFM edge.

Our first-principles stress calculations confirm qualitatively the recent empirical-potential results [10] that both edges are under compressive stress. However, there are also some significant differences. Two quantum manifestations of edge stress stand out, which are absent from the empirical prediction. One is the quantum oscillation of armchair edge stress, and the other is the spin reduction of zigzag edge stress. The physical origin of edge energy and edge stress is associated with the formation of one dangling bond on each edge atom. The repulsive interaction between the dangling bonds is believed to be one origin for the "compressive" edge stress. In addition, in the armchair edge, it is well-known [20] that the edge dimers form triple $-$C≡C$-$ bonds with a much shorter distance ∼1.23 eV/Å (according to our calculation) adding extra compressive stress to the edge, while in the zigzag edge, spin polarization further reduces the compressive stress. Consequently, the armchair edge has a much larger compressive stress ~ -1.45 eV/Å than the zigzag edge ~ -0.5 eV/Å, in contrast to the empirical prediction of a smaller compressive stress in the armchair edge (~ -1.05 eV/Å) than in the zigzag edge (~ -2.05 eV/Å) [10].

The quantum effects in edge stress will in turn modify the mechanical edge instability. The compressive edge stress means the edge has a tendency to stretch. If we apply a uniaxial in-plane strain to a nanoribbon along the edge direction, the strain energy can be calculated as [10]

$$E_{str} = 2\tau_e L\varepsilon + E_e L\varepsilon^2 + \frac{1}{2}E_s A\varepsilon^2 \tag{3.1}$$

Here, A is the ribbon area, L is the edge length, τ_e is the edge stress, E_e is the 1D edge elastic modulus in a 2D nanoribbon, in analogy to the 2D surface elastic modulus in a 3D nanofilm [21], and E_s is the 2D sheet elastic modulus. Since τ_e is negative, for small enough tensional strain ε (positive), the negative first term (linear to ε) in Eq. 3.1 can always overcome the positive second and third terms (quadratic to ε) to make E_{str} negative. So, the ribbon is unstable against a small amount of stretching along the edge direction.

Fitting first-principles calculations, by manually deforming the sheet and ribbon along the edge direction, to Eq. 3.1, we obtained E_s ≈21.09 eV/Å^2, E_e(armchair)≈3 eV/Å and E_e(zigzag)≈24 eV/Å with τ_e already calculated directly (see Figs. 3.1 and 3.2). Our E_s value is in good agreement with the experiment [22] and empirical result [10], but E_e is notably different from the empirical results [10].

Another effective way to stretch the edge of a 2D sheet is by out-of-plane edge twisting and warping motions, which are barrierless processes. For example, assuming a sinusoidal edge warping with displacement $\mu_e = asin(2\pi x/\lambda)$ of amplitude a and wavelength λ, which decays exponentially into the sheet as $e^{-y/l}$ (see inset of Figure 3.3), where l is the decay length, Shenoy et al. have shown that minimization of strain energy leads to characteristic length scales of such warping instability as $l \approx 0.23\lambda$ and $a \approx \sqrt{(-\lambda\tau_e)/(1.37E_b + 14.8E_e/\lambda)}$. Using their empirical-potential values of τ_e, E_e, and E_s, they estimated that the warping magnitude of the armchair edge is smaller than that of the zigzag edge, and both are larger than typical thermal fluctuations [10].

Our first-principles predictions, however, are different in several ways. First, absent from empirical prediction, the quantum oscillation of the τ_e of the armchair edge gives rise to an oscillating armchair edge warping amplitude for a given wavelength as a function of nanoribbon width, as shown in Figure 3.3(a). Second, the mechanical undulation of zigzag edges induced by compressive edge stress is comparable to thermal fluctuations [3,4], as shown in Figure 3.3(b), and hence, the two are difficult to distinguish.

Because the compressive edge stress is partly originated from the dangling bond, naturally, we may saturate the dangling bonds to relieve the compressive stress. We have tested this idea by saturating the edge with H that indeed confirmed our physical intuition. For the armchair edge in a 1nm wide ribbon, we found H saturation changes the edge stress from −1.42 eV/Å to −0.35 eV/Å; for the zigzag edge in a 2.0 nm wide ribbon, it changes the edge stress from −0.42 eV/Å to +0.13 eV/Å. Thus, the H edge saturation, or saturation by other molecules in general, is expected to relieve the edge compression and even reverse the compressive stress in a zigzag edge to tensile.

3.3 Edge Reconstruction and Adsorption

Surface reconstruction has long been known as an effective mechanism in relieving surface stress [23]. Thus, we have also investigated possible edge reconstructions in relieving the edge compressive stress. The Stone-Wales (SW) defect [24] appealed to us because a SW defect in 2D is equivalent to a dislocation core in 3D that is known as a common stress relief mechanism. Figure 3.4(a) shows the calculated armchair edge stress along with edge

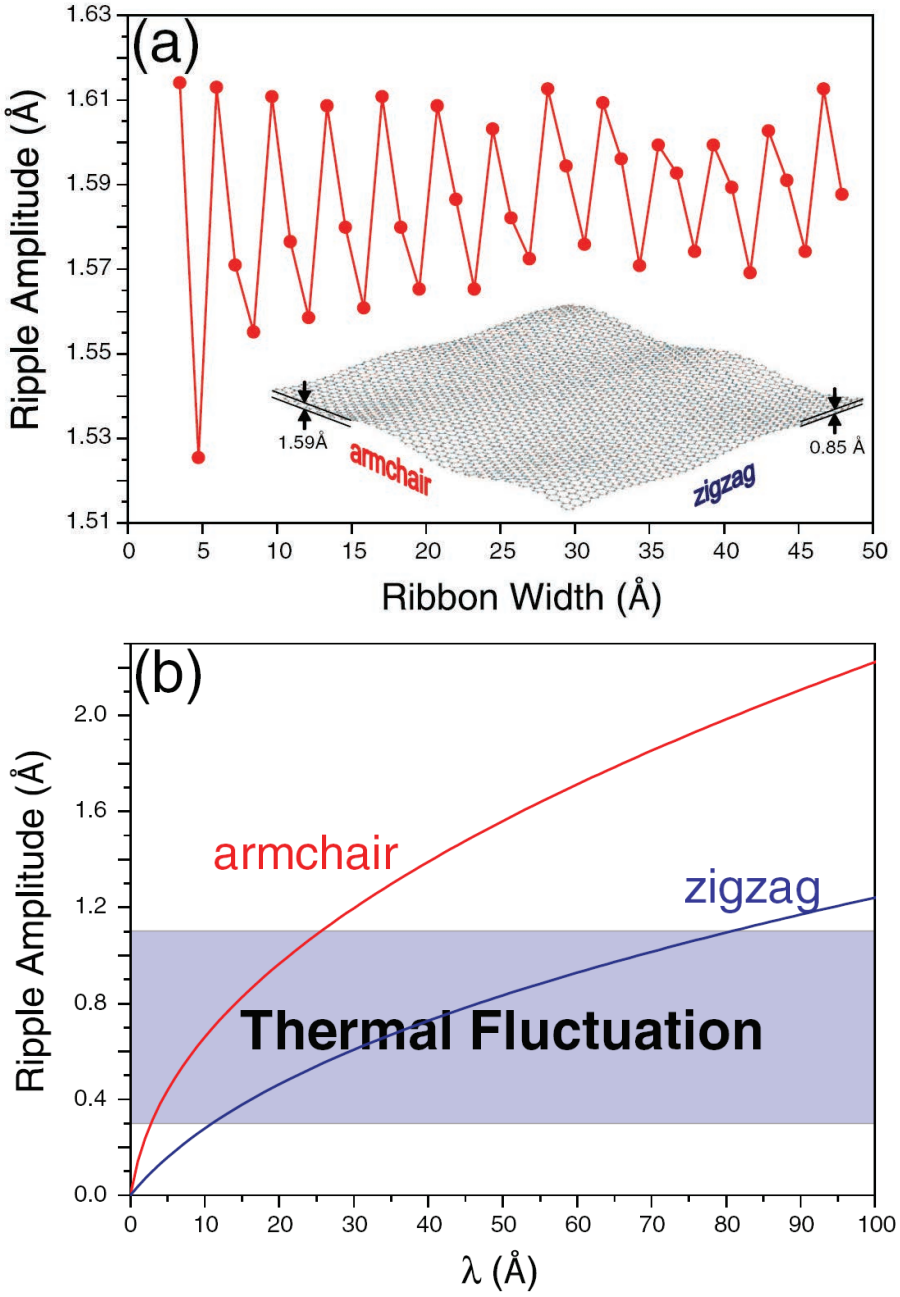

Figure 3.3. Ripple amplitude along graphene edge (a) Armchair edge ripple amplitude versus ribbon width for λ=50Å. Inset: Schematics of ripple formation along the armchair and zigzag edge. (b) Armchair and zigzag edge ripple amplitude as a function of λ. Light blue band shows the typical range of thermal fluctuation.

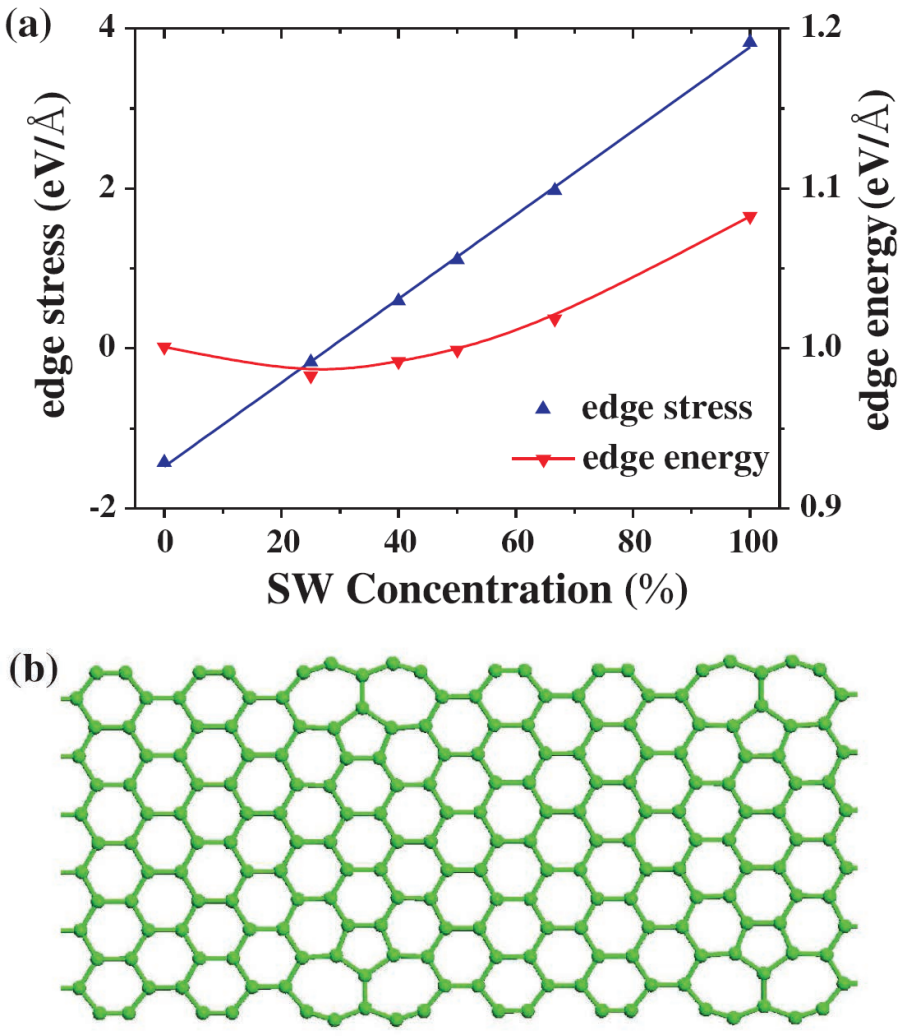

Figure 3.4. Edge reconstruction as a stress relief mechanism: (a) The armchair edge stresses (with linear fit) and edge energies as a function of edge SW defect concentration. (b) The optimized ribbon structure at the 50% SW defect concentration.

energy as a function of one type of SW defect (7-5-7 ring structure) concentration. Figure 3.4(b) shows an example of the optimized edge structure at the 50% defect concentration. The edge stress increases linearly from compressive to tensile with the increasing SW defect concentration. The most stable edge structure is at ∼25% defect concentration where the edge stress is very small and slightly compressive. A small stress value indicates that this chemically stable edge structure (with the lowest edge energy) is also most mechanically stable against deformation.

Figure 3.5(a) shows the ground state AF zigzag edge stress along with edge energy as a function of another type of SW defect (5-7 ring structure) concentration. Figure 3.5(b) shows an example of the optimized edge structure and spin charge density at the 50% defect concentration. The edge stress increases linearly from compressive to tensile with the increasing defect concentration, the same as the case of the armchair edge [Figure 3.4(a)], but the edge energy decreases monotonically with the most stable edge having 100% of defects, in agreement with a recent first-principles calculation [8]. The initial compressive edge stress (~ -0.5 eV/Å) is completely reversed to a large tensile value of ∼1.2 eV/Å in the most stable edge. Also, the 100% defected edge becomes non-spin-polarized. In general, the zigzag edge spin decreases continuously with the increasing SW defect concentration, similar to the behavior found previously for other types of defects [25].

3.4 Conclusion

In conclusion, quantum effects have been widely shown for electronic structures and energetic quantities of low-dimensional nanostructures. We demonstrate, in addition, quantum manifestations of mechanical quantities in graphene edge stress. We show that quantum confinement can lead to stress oscillations, and spin polarization can reduce stress, which in turn "quantum mechanically" modifies the edge twisting and warping instability. We further show that H edge saturation and SW edge reconstruction cannot only improve the "chemical" stability of graphene edges by lowering the edge energy, but also enhance their "mechanical" stability by converting compressive edge stress towards tensile and hence stabilizing the planar edge structure. Our first-principles findings, which cannot be captured by classical methods, provide new insights into the understanding of mechanical stability of graphene. We expect the quantum manifestation of mechanical properties such as stress to exist generally in many low-dimensional nanostructures.

Indeed, after the original work of graphene edge stress, our group has developed a rigorous theoretical framework underlying a new concept of "quantum electronic stress

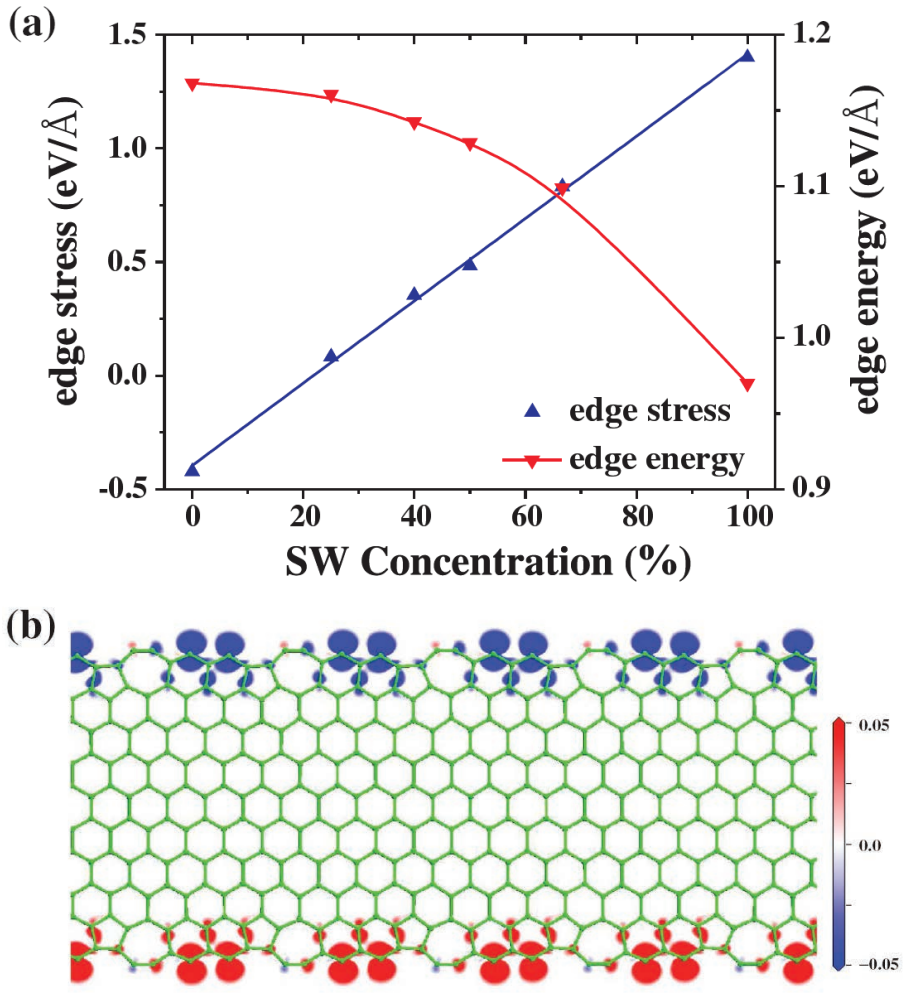

Figure 3.5. Edge reconstruction as a stress relief mechanism: (a) The zigzag edge stresses (with linear fit) and edge energies as a function of SW defect concentration. (b) The optimized ribbon structure and spatial distribution of spin density (charge density difference between spin-up and spin-down states in units of μ_BÅ^{-2}) of the AFM ground state at the 50% SW defect concentration.

(QES)" [27], based on density functional theory, which describes the lattice stress purely induced by electronic excitation and perturbation in the absense of lattice strain. Junyi Zhu studied QES induced by charge doping (electrons or holes) in semiconductors and proposed a strategy to enhance doping by strain [28,29]. Miao Liu studied surface QES induced by quantum size effect in metal nanofilms [30,31], similar to edge stress discussed here.

3.5 References

[1] A. H. Castro Neto et al., Rev. Mod. Phys. **81**, 109 (2009).

[2] A. K. Geim and K. S. Novoselov, Nature Mater. **6**, 183 (2007).

[3] J. C. Meyer et al., Nature (London) **446**, 60 (2007).

[4] A. Fasolino, J. H. Los, and M. I. Katsnelson, Nature Mater. **6**, 858 (2007).

[5] M. S. Gass et al., Nature Nanotech. **3**, 676 (2008).

[6] L. D. Landau, Phys. Z. Sowjetunion **11**, 26 (1937).

[7] N. D. Mermin, Phys. Rev. **176**, 250 (1968).

[8] P. Koskinen, S. Malola, and H. Hakkinen, Phys. Rev. Lett. **101**, 115502 (2008).

[9] T. Wassmann et al., Phys. Rev. Lett. **101**, 096402 (2008).

[10] V. B. Shenoy, C.D. Reddy, A. Ramasubramaniam, and Y.W. Zhang, Phys. Rev. Lett. **101**, 245501 (2008).

[11] F. Liu, M. Hohage, and M. G. Lagally, in Encyclopedia of Applied Phys., edited by H. Immergut and G. Trigg, Supplement Vol. **321**, (Wiley-VCH, New York, 1999).

[12] R. Pala and F. Liu, J. Chem. Phys. **120**, 7720 (2004).

[13] G. Kresse and J. Furthmuller, Comput. Mater. Sci. **6**, 15 (1996).

[14] O. H. Nielsen and R. M. Martin, Phys. Rev. B **32**, 3780 (1985).

[15] K. Nakada et al., Phys. Rev. B **54**, 17954 (1996).

[16] K. Wakabayashi et al., Phys. Rev. B 59, 8271 (1999).

[17] Y.-W. Son, M. L. Cohen, and S. G. Louie, Phys. Rev. Lett. **97**, 216803 (2006).

[18] Q. Yan et al., Nano Lett. **7**, 1469 (2007).

[19] H. Lee et al., Phys. Rev. B **72**, 174431 (2005).

[20] T. Kawai, Y. Miyamoto, O. Sugino, and Y. Koga, Phys. Rev. B **62**, R16349 (2000).

[21] J. Zang and F. Liu, Nanotechnology 18, 405501 (2007); Appl. Phys. Lett. **92**, 021905 (2008).

[22] C. Lee et al., Science **321**, 385 (2008).

[23] F. Liu and M. G. Lagally, Phys. Rev. Lett. **76**, 3156 (1996).

[24] A. J. Stone and D. J. Wales, Chem. Phys. Lett. **128**, 501 (1986).

[25] B. Huang et al., Phys. Rev. B **77**, 153411 (2008).

[26] K.V. Bets and B. I. Yakobson, Nano Res. **2**, 161 (2009).

[27] H. Hu, M. Liu, Z. F. Wang, J. Zhu, D. Wu, H. Ding, Z. Liu, and F. Liu, Phys. Rev. Lett. **109**, 055501 (2012).

[28] J. Zhu, F. Liu, and M. A. Scarpulla, APL Mater. **2**, (2014).

[29] J. Zhu, F. Liu, G. B. Stringfellow, and S.-H. Wei, Phys. Rev. Lett. **105**, 195503 (2010).

[30] M. Liu, Y. Han, L. Tang, J.-F. Jia, Q.-K. Xue, and F. Liu, Phys. Rev. B **86**, 125427 (2012).

[31] M. Liu and F. Liu, Nanotechnology **25**, 135706 (2014).

CHAPTER 4

PREDICTION OF 2D ORGANIC TOPOLOGICAL INSULATOR

4.1 Introduction

The concept of topological order in condensed matter physics provides a new perspective for understanding the origin of different quantum phases and has generated intense recent interest in searching for nontrivial topological materials, so-called topological insulators (TIs)[1-13]. The defining signature of a 2D (3D) TI is its nontrivial bulk band topology around a global SOC gap with corresponding topological edge (surface) states within the SOC gap. These characteristic edge (surface) states have a topological origin, which are protected from elastic backscattering and localization, and hence hold potential for applications in spintronics and quantum computation devices. To date, all of the experimentally confirmed TIs are based on inorganic materials[1-13]. Recently, theories have predicted the possible existence of OTI in 2D organometallic frameworks[14-16], but those theoretically proposed structures remain to be synthesized in the experiments.

In this work, we report the identification of nontrivial topological states in an experimental sample of 2D organometallic framework, $Ni_3C_{12}S_{12}$ lattice (Figure 4.1), recently synthesized by Kambe et al. [17]. First-principles calculations of band structure, edge state, Chern number, and spin Hall conductance are performed to reveal the nontrivial topology in this lattice structure. A single-orbital tight-binding (TB) model is also given to illustrate its SOC gap opening mechanism.

4.2 Methodology

First-principles calculations are carried out within the framework of the Perdew-Burke-Ernzerhof generalized gradient approximation using VASP [18]. All the calculations are performed with a plane-wave cutoff of 500 eV on the 7×7×1 Monkhorst-Pack k-point mesh. The vacuum layer is 15 Å thick to ensure decoupling between neighboring slabs. During structural relaxation, all atoms are relaxed until the forces are smaller than 0.01 eV/Å.

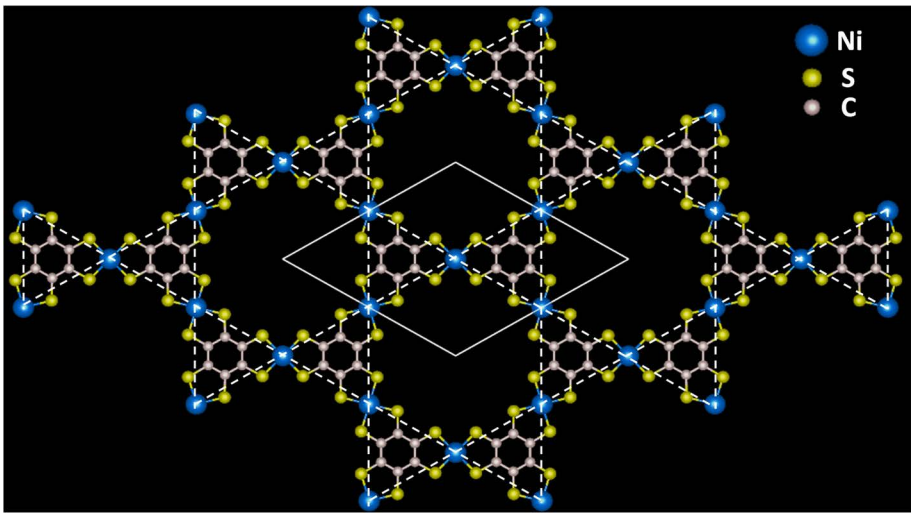

Figure 4.1. Atomic structure of the $Ni_3C_{12}S_{12}$ lattice. The solid lines show the unit cell, and the dashed lines outline the kagome lattice.

4.3 Topological Edge States in $Ni_3C_{12}S_{12}$ Lattice

Figure 4.1 shows the optimized 2D $Ni_3C_{12}S_{12}$ lattice structure, which adopts a kagome lattice. The optimized lattice constant is found to be L=14.63 Å, in good agreement with the experimental value (14∼15Å) [17]. Figure 4.2a shows the band structure of $Ni_3C_{12}S_{12}$ lattice with SOC around the Fermi level. We can clearly see the typical kagome bands as shown previously in a TB model [19], consisting of one flat band above two Dirac bands (top three red bands in Figure 4.2a, all of the bands are spin degenerated), which are well separated from the other black bands. Figure 4.2b shows the zoom-in band structures of the three kagome bands. The band gap of the Dirac band is Δ_1=13.6 meV, while the band gap between the flat band and the top branch of the Dirac band is δ_2=5.8 meV. Both Δ_1 and Δ_2 vanish in the absence of SOC from the first-principles calculations.

We then checked the edge states of the $Ni_3C_{12}S_{12}$ lattice, since the existence of topological edge states is an important signature of the 2D TIs. The edge states of the $Ni_3C_{12}S_{12}$ lattice is calculated by using the Wannier90 package [20], in which a TB Hamiltonian in the basis of the maximally localized Wannier functions (MLWFs) is fitted to the first-principles band structures. Using these MLWFs, the edge Green's function of the semi-infinite lattice is constructed using the recursive method [21] and the local density of state (LDOS) of the edge is calculated. This method provides a direct connectivity between the edge states and the bulk states. The LDOS of a semi-infinite $Ni_3C_{12}S_{12}$ lattice is shown in Figure 4.2c and d for spin-up and spin-down components, respectively, where one can see the nontrivial topological edge states that connect the bulk states and form a 1D Dirac cone in both SOC gaps (Δ_1 and Δ_2). In addition, the spin-up and spin-down edge states have inverse group velocity, which will propagate along opposite directions along the edge, as required for the 2D TI states.

We stress that the kagome bands of the $Ni_3C_{12}S_{12}$ lattice represent a real material system that realizes the single-orbital TB model on a kagome lattice as proposed by Tang et al. [19]. The corresponding model Hamiltonian in the reciprocal space can be expressed as follows:

$$H = \begin{pmatrix} E_0 & 2t_1\cos k_1 & 2t_1\cos k_2 \\ 2t_1\cos k_1 & E_0 & 2t_1\cos k_3 \\ 2t_1\cos k_2 & 2t_1\cos k_3 & E_0 \end{pmatrix} \pm i2\lambda_1 \begin{pmatrix} 0 & \cos k_1 & -\cos k_2 \\ -\cos k_1 & 0 & \cos k_3 \\ \cos k_2 & -\cos k_3 & 0 \end{pmatrix} \quad (4.1)$$

where $\overrightarrow{a_1} = (L/2)\hat{x}$, $\overrightarrow{a_2} = (L/2)[(\hat{x} + \sqrt{3}\hat{y}]/2$, $\overrightarrow{a_3} = \overrightarrow{a_2} - \overrightarrow{a_1}$, $k_n = \overrightarrow{k} \cdot \overrightarrow{a_n}$, and L is the lattice constant. E_0 is the on-site energy, t_1 is the nearest-neighbor hopping parameter, λ_1 is the

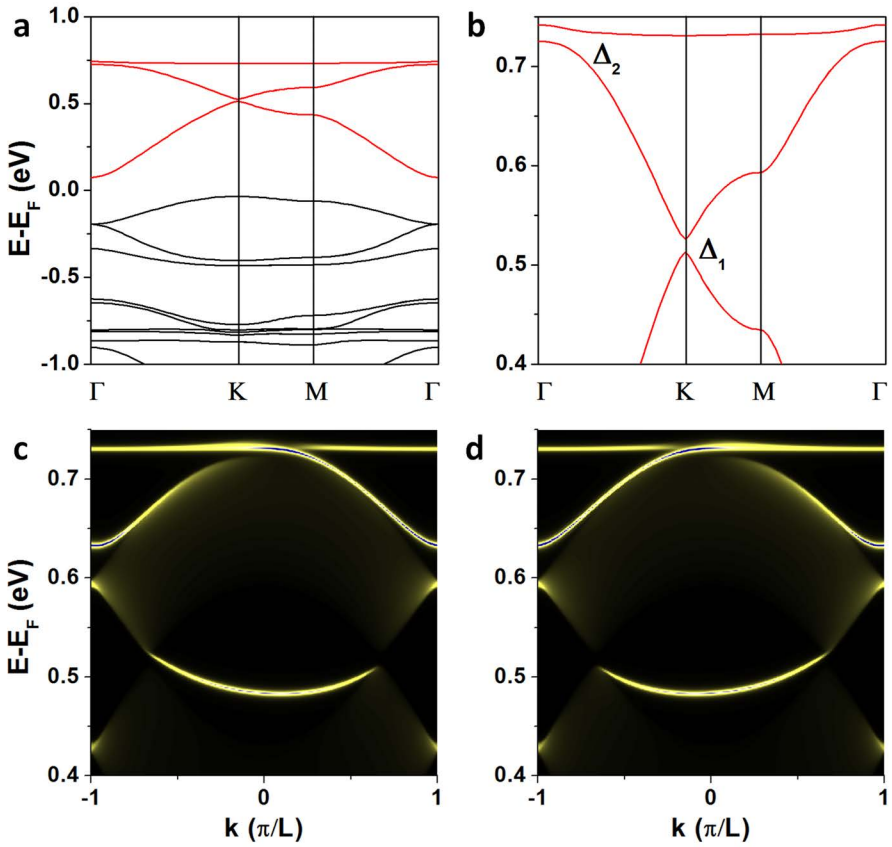

Figure 4.2. Band structure of the $Ni_3C_{12}S_{12}$ lattice. (a) 2D band structure of the $Ni_3C_{12}S_{12}$ lattice along the high symmetry directions. (b) The zoom-in kagome bands around two SOC gaps. (c and d) The semi-infinite edge states for the spin-up and spin-down components, respectively. Overlapping c and d would give the 1D edge Dirac band in both SOC gaps as in Figure 4.4b.

nearest-neighbor intrinsic SOC and +(−) refers to the spin-up (spin-down) bands. The corresponding fitting parameters for the $Ni_3C_{12}S_{12}$ lattice are $E_0 = 0.59$ eV, $t_1 = -0.07$ eV, and $\lambda_1 = 0.0035$ eV, which show very good agreement with the first-principles results (Figure 4.3a). The TB model analysis indicates that the SOC gaps (Δ_1 and Δ_2) in the $Ni_3C_{12}S_{12}$ lattice are opened due to the intrinsic SOC of d-orbits of Ni atoms, given the inversion lattice symmetry that excludes the Rashba SOC effect.

To further confirm the nontrivial topology of the $Ni_3C_{12}S_{12}$ lattice, the Chern number (C) and spin Chern number (C^s) are calculated using the Kubo formula [22,23] as follows:

$$C = \frac{1}{2\pi}\int_{BZ} \mathrm{d}^2\overrightarrow{k}\,\Omega(\overrightarrow{k}) \tag{4.2}$$

$$\Omega(\overrightarrow{k}) = \sum_n f_n \Omega_n(\overrightarrow{k}) \tag{4.3}$$

$$\Omega_n(\overrightarrow{k}) = -\sum_{n'\neq n} 2\,\mathrm{Im}\,\frac{\langle\Psi_{nk} \mid \nu_x \mid \Psi_{n'k}\rangle\langle\Psi_{n'k} \mid \nu_y \mid \Psi_{nk}\rangle}{(\varepsilon_{n'k} - \varepsilon_{nk})^2} \tag{4.4}$$

$$C^s = \frac{1}{2\pi}\int_{BZ} \mathrm{d}^2\overrightarrow{k}\,\Omega^s(\overrightarrow{k}) \tag{4.5}$$

$$\Omega^s(\overrightarrow{k}) = \sum_n f_n \Omega^s_n(\overrightarrow{k}) \tag{4.6}$$

$$\Omega^s_n(\overrightarrow{k}) = -\sum_{n'\neq n} 2\,\mathrm{Im}\,\frac{\langle\Psi_{nk} \mid j_x \mid \Psi_{n'k}\rangle\langle\Psi_{n'k} \mid \nu_y \mid \Psi_{nk}\rangle}{(\varepsilon_{n'k} - \varepsilon_{nk})^2} \tag{4.7}$$

where n is the band index, Ψ_{nk} are the eigenstate of eigenvalue ε_{nk} of band n, f_n is the Fermi distribution function, $\nu_{x/y}$ is the velocity operator, j_x is the spin current operator

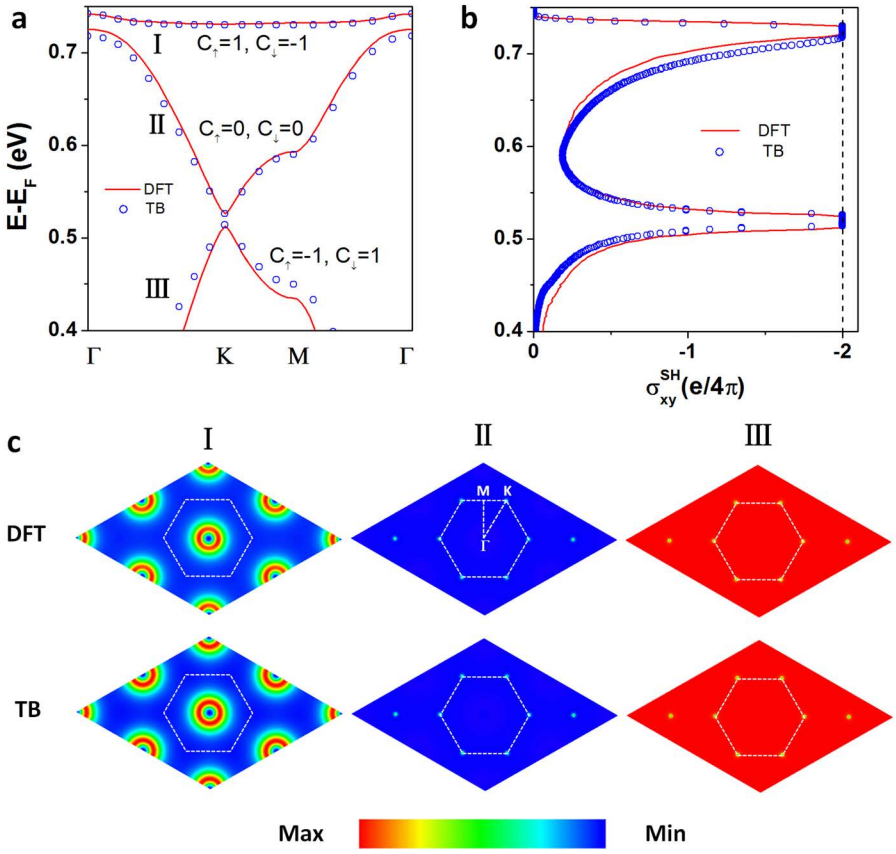

Figure 4.3. Evidences of topological states in the $Ni_3C_{12}S_{12}$ lattice. (a) A comparison between first-principles and single-orbital TB band structures for the flat (I) and Dirac (II and III) bands. (b) Same as a for the quantized spin Hall conductance within the energy window of the two SOC gaps. (c) Spin Berry curvatures in the reciprocal space for flat (left column) and Dirac bands (right two columns). The dashed lines mark the first Brillouin zone.

defined as $(s_z\nu_x + \nu_x s_z)/2$, and s_z is the spin operator. The Chern number and spin Chern number are defined as

$$C = C_\uparrow + C_\downarrow \quad C^s = \frac{1}{2}(C_\uparrow - C_\downarrow) \tag{4.8}$$

From Eqs. (4.2)-(4.8), the Chern number of each band with different spins is calculated, as marked in Figure 4.3a. For both spins, the flat band and the bottom Dirac band have a nonzero Chern number (± 1), while the top Dirac band has a zero Chern number. Thus, within the SOC gap of Δ_1 or Δ_2, the Chern number is zero, but the spin Chern number is -1, indicating that the $Ni_3C_{12}S_{12}$ lattice is topologically nontrivial.

The coexistence of two TI states, one from Dirac band and the other from flat band, at different energies can manifest in transport measurement. The spin Hall conductance can be obtained from the spin Chern number as

$$\sigma_{xy}^{SH} = \frac{e}{4\pi}(C_\uparrow - C_\downarrow) \tag{4.9}$$

Figure 4.3b shows the calculated spin Hall conductance as a function of energy using the first-principles and single-orbital TB method, which has a quantized value ($-2e/4\pi$) within the energy window of both SOC gaps.

We also compare the calculated spin Berry curvature in Figure 4.3c, showing very good agreement between the first-principles method and the single-orbital TB model. The spin Berry curvature of the flat band is mainly around the Γ point (Figure 4.3c, left column), while that of the Dirac bands is around the K point (Figure 4.3c, right two columns). This again confirms that the $Ni_3C_{12}S_{12}$ lattice represents a real organometallic lattice to realize the original kagome model proposed by Tang et al. [19], which has an interesting flat band with nonzero Chern number. By including many-body interactions in such a nontrivial flat band, the fractional quantum Hall effect can also be realized [24].

4.4 Tunability of $Ni_3C_{12}S_{12}$ Lattice

One distinct advantage of organic topological materials is their high tunability by using different metal atoms and molecular ligands. In addition to examining the experimentally made $Ni_3C_{12}S_{12}$ lattice, we also tested the $Au_3C_{12}S_{12}$ lattice by replacing Ni with Au to demonstrate the tunability of such lattices. The optimized lattice constant of $Au_3C_{12}S_{12}$ lattice is found to be L=15.09 Å. Its band structure with SOC and semi-infinite edge states are shown in Figure 4.4a and b, respectively. Overall, the band structure and topology of

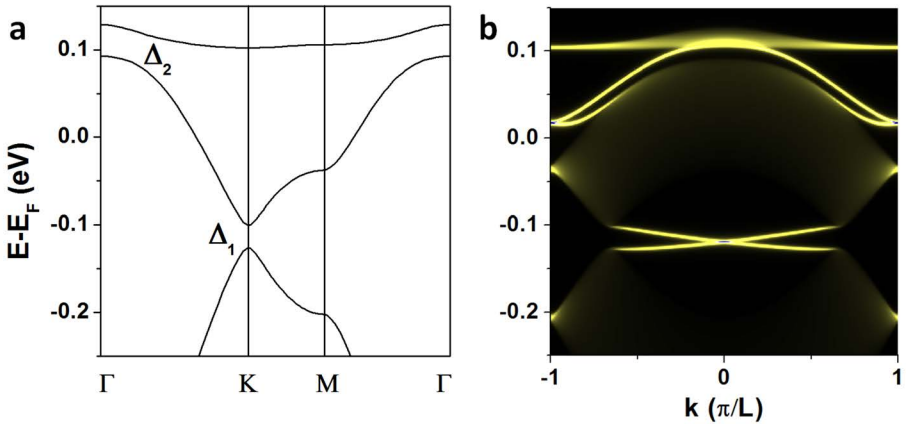

Figure 4.4. Topological states in the $Au_3C_{12}S_{12}$ lattice. (a) Band structure of the $Au_3C_{12}S_{12}$ lattice. (b) The semi-infinite Dirac edge states (both spin-up and spin-down components) within the SOC gaps.

the $Au_3C_{12}S_{12}$ lattice are physical same as those of the $Ni_3C_{12}S_{12}$ lattice, except that the Fermi level is now located in between the flat band and the Dirac point and the SOC gaps are larger with Δ_1=22.7 meV and Δ_2=9.5 meV.

We note that the Fermi level is not in the SOC gaps in both lattices, so doping is needed. This requires doping one electron (or one hole) per unit cell in the $Au_3C_{12}S_{12}$ lattice and two (or four) electrons in the $Ni_3C_{12}S_{12}$ lattice, respectively, which corresponds to a doping concentration of $\sim 5\times10^{13}$ cm^{-2} to $\sim 2\times10^{14}$cm^{-2}. In our first-principles calculations, the doping effect can be studied by removing (or adding) electrons from (or to) the lattice, and meanwhile adding a homogeneous background charge neutrality, as done before for other proposed OTIs [14]. In experiments, the doping effect can be achieved by the electrostatic gating. Recent experiment has demonstrated that the doping concentration in graphene can be achieved up to 4×10^{14}cm^{-2} for both electrons and holes by using a solid polymer electrolyte gate [25].

Our predicted 2D OTI would offer several advantages over their inorganic counterparts. First of all, they should be less sensitive against oxidation, which would strong simplify the device fabrication. Furthermore, the possibility to implement a wide variety of metal ions and organic ligand will enable specific tailoring of the electronic properties of OTI. Our recent work has already demonstrated such possibility to tune an OTI made of $Bi_2C_{18}H_{12}$ lattice into a magnetic OTI by substituting Bi with Mn atoms, and a quantum anomalous Hall effect having an odd Chern number is shown to be realizable in this magnetic OTI [16]. Therefore, it is reasonable to anticipate similar magnetic OTIs to be realized in the $Ni_3C_{12}S_{12}$ lattice by substituting Ni with other transition metal elements with large exchange energy.

4.5 Conclusion

In conclusion, using first-principles calculations, we identify a real OTI material in a recent experimentally synthesized 2D organometallic framework, which provides a viable approach for searching new TIs in organic materials. We envision that more OTIs will be discovered in the future, which will greatly broaden the scientific and technological impact of TIs.

4.6 Reference

[1] M. Z. Hasan and C. L. Kane, Rev. Mod. Phys. **82**, 3045 (2010).

[2] X.-L. Qi and S.-C. Zhang, Rev. Mod. Phys. **83**, 1057 (2011).

[3] C. L. Kane and E. J. Mele, Phys. Rev. Lett. **95**, 226801 (2005).

[4] L. Fu and C. L. Kane, Phys. Rev. B **76**, 045302 (2007).

[5] B. A. Bernevig, T. L. Hughes, and S.-C. Zhang, Science **314**, 1757 (2006).

[6] M. Knig, S. Wiedmann, C. Brne, A. Roth, H. Buhmann, L. W. Molenkamp, X.-L. Qi, and S.-C. Zhang, Science **318**, 766 (2007).

[7] P. Gehring, H. M. Benia, Y. Weng, R. Dinnebier, C. R. Ast, M. Burghard, and K. Kern, Nano Lett. **13**, 1179 (2013).

[8] H. Li, J. Cao, W. Zheng, Y. Chen, D. Wu, W. Dang, K. Wang, H. Peng, and Z. Liu, J. Am. Chem. Soc. **134**, 6132 (2012).

[9] L. Mchler, H. Zhang, S. Chadov, B. Yan, F. Casper, J. Kbler, S.-C. Zhang, and C. Felser, Angew. Chem., Int. Ed. **51**, 7221 (2012).

[10] Z. Liu, C.-X. Liu, Y.-S. Wu, W.-H. Duan, F. Liu, and J. Wu, Phys. Rev. Lett. **107**, 136805 (2011).

[11] F. Yang, L. Miao, Z. F. Wang, M.-Y. Yao, F. Zhu, Y. R. Song, M.-X. Wang, J.-P. Xu, A. V. Fedorov, Z. Sun, G. B. Zhang, C. Liu, F. Liu, D. Qian, C. L. Gao, and J.-F. Jia, Phys. Rev. Lett. **109**, 016801 (2012).

[12] L. Miao, Z. F. Wang, W. Ming, M.-Y. Yao, M. Wang, F. Yang, Y. R. Song, F. Zhu, A. V. Fedorov, Z. Sun, C. L. Gao, C. Liu, Q.-K. Xue, C.-X. Liu, F. Liu, D. Qian, and J.-F. Jia, Proc. Natl. Acad. Sci. U.S.A. **110**, 2758 (2013).

[13] Z. Wang, M.-Y. Yao, W. Ming, L. Miao, F. Zhu, C. Liu, C. Gao, D. Qian, J.-F. Jia, and F. Liu, Nat. Commun. **4**, 1384 (2013).

[14] Z. Wang, Z. Liu, and F. Liu, Nat. Commun. **4**, 1471 (2013).

[15] Z. Liu, Z.-F. Wang, J.-W. Mei, Y.-S. Wu, and F. Liu, Phys. Rev. Lett. **110**, 106804 (2013).

[16] Z. F. Wang, Z. Liu, and F. Liu, Phys. Rev. Lett. **110**, 196801 (2013).

[17] T. Kambe, R. Sakamoto, K. Hoshiko, K. Takada, M. Miyachi, J.-H. Ryu, S. Sasaki, J. Kim, K. Nakazato, M. Takata, and H. Nishihara, J. Am. Chem. Soc. **135**, 2462 (2013).

[18] G. Kresse and J. Hafner, Phys. Rev. B **47**, 558 (1993).

[19] E. Tang, J.-W. Mei, and X.-G. Wen, Phys. Rev. Lett. **106**, 236802 (2011).

[20] A. A. Mostofi, J. R. Yates, Y.-S. Lee, I. Souza, D. Vanderbilt, and N. Marzari, Comput. Phys. Commun. **178**, 685 (2008).

[21] M. P. L. Sancho, J. M. L. Sancho, J. M. L. Sancho, and J. Rubio, J. Phys. F **15**, 851 (1985).

[22] Y. Yao, L. Kleinman, A. H. MacDonald, J. Sinova, T. Jungwirth, D. Wang, E. Wang, and Q. Niu, Phys. Rev. Lett. **92**, 037204 (2004).

[23] Y. Yao and Z. Fang, Phys. Rev. Lett. **95**, 156601 (2005).

[24] D. Sheng, Z.-C. Gu, K. Sun, and L. Sheng, Nat. Commun. **2**, 389 (2011).

[25] D. K. Efetov and P. Kim, Phys. Rev. Lett. **105**, 256805 (2010).

CHAPTER 5

PREDICTION OF LARGE GAP FLAT CHERN BAND IN A TWO-DIMENSIONAL ORGANIC FRAMEWORK

5.1 Introduction

The recently proposed flat Chern band (FCB) in two-dimensional (2D) structures [1-3] is featured with both exotic dispersion and topological order, which are signatures of graphene [4,5] and topological insulator [6,7], respectively. By definition, the bandwidth of a FCB is smaller than both the energy gap between the FCB and other bands and the interaction energy scale [1-3]. Kinetic energy of carriers in the FCB is strongly suppressed. As a consequence, strong Coulomb interaction between carriers is expected in addition to the topological frustration that together spawn unprecedented topological strongly correlated electronic states [8-10]. Moreover, a nontrivial Chern variant is required for FCB, which is the fundamental difference between FCB and the narrow band in heavy fermion compounds. A flat band with nontrivial Chern variant is a consequence from a well-balanced effect of lattice hopping, SOC, and ferromagnetism. Because of the rigorous criteria, except for the theoretical model proposed in Ref [1-3], no real material has been proposed until very recent when the concept of organic topological insulator was first proposed [11,12]. Based on the same theme, a two-dimensional organometallic framework so-called indium-phenylene organometallic framework (IPOF) was designed to realize FCB as well [13]. However, due to the weak SOC within indium ions, the IPOF has a fairly small SOC gap, which is around 30 meV. In this work, we present a first-principles design to enlarge the SOC gap of a 2D organometallic framework with nontrivial FCB by replacing indium with thallium, which has stronger SOC than IPOF while maintaining the symmetry and topology of IPOF.

5.2 Methodology

Our first-principles calculations are carried out within the framework of the Perdew-Burke-Ernzerhof generalized gradient approximation using VASP [14]. All of the calcula-

tions are performed with a plane-wave cutoff of 600 eV on the 11×11×1 Monkhorst-Pack k-point mesh. The vacuum layer is chosen to be 20 Å thick to ensure decoupling between neighboring slabs. During structural relaxation, all atoms are relaxed until the forces are smaller than 0.01 eV/Å.

5.3 Large Gap Topological Edge States in Tl_2Ph_3 Lattice

Figure 5.1 shows the optimized 2D atomic structure of the Tl_2Ph_3 lattice, which adopts a hexagonal lattice by binding p-orbital heavy elements (Tl) with organic ligands (paraphenylene groups). The dashed yellow lines show the unit cell, which contains two Tl ions and three paraphenylene groups and has a lattice constant of 12.70 . It is worth noting that the Tl_2Ph_3 lattice resembles the already synthesized organic framework with only Tl ions replaced by boroxine rings [15,16].

Figure 5.2b shows both the band structure on a path intersecting several high symmetry points as labelled in Figure 5.2a and atomic-orbital projected density of states (APDOS) of the Tl_2Ph_3 lattice without SOC. The band structure indicates that the Tl_2Ph_3 lattice is a nonmagnetic insulator with a band gap of about 2.5 eV. The four signature bands indicated by Ref [13] can be clearly seen in the valence zone near Fermi level, consisting of two nearly flat bands sandwiching two dispersive bands with a Dirac cone formed at the K point. The top and bottom flat bands are nearly flat in the whole Brillouin zone with a narrow bandwidth of 12 meV and 33 meV, respectively. The flat bands and the dispersive bands touch each other at the Γ point. Moreover, there are also six bands within the range between the top and bottom flat bands, which come from the p_z orbitals of C and Tl atoms. Comparing Figure 5.2b with the results shown in Ref [13], the most significant difference is that the Dirac cone at the K point formed by the two dispersive bands is now well separated from the six p_z bands. We expect that a SOC gap will open at the Dirac cone and a nontrivial semi-infinite edge states will be found within the gap.

Then, we include SOC in the first-principles calculation, and the results are shown in Figure 5.2c. Comparing Figure 5.2c with Figure 5.2b, the degenerated Γ and K points of the four bands are now split, which result in finite gap at these points. The band gap of the Dirac band is Δ^{23}=255 meV, while the direct and indirect band gap between the top flat band and the top branch of the dispersive bands is Δ^{12}_{dir}=284 meV and Δ^{12}_{ind}=143 meV, respectively. The separation between the top and bottom flat bands is Δ_{14}=1.3 eV. Also, in the presence of SOC, the bandwidth of the top and bottom flat bands increases from 12 meV and 33 meV to 140 meV and 89 meV, respectively. We note that all the bands are

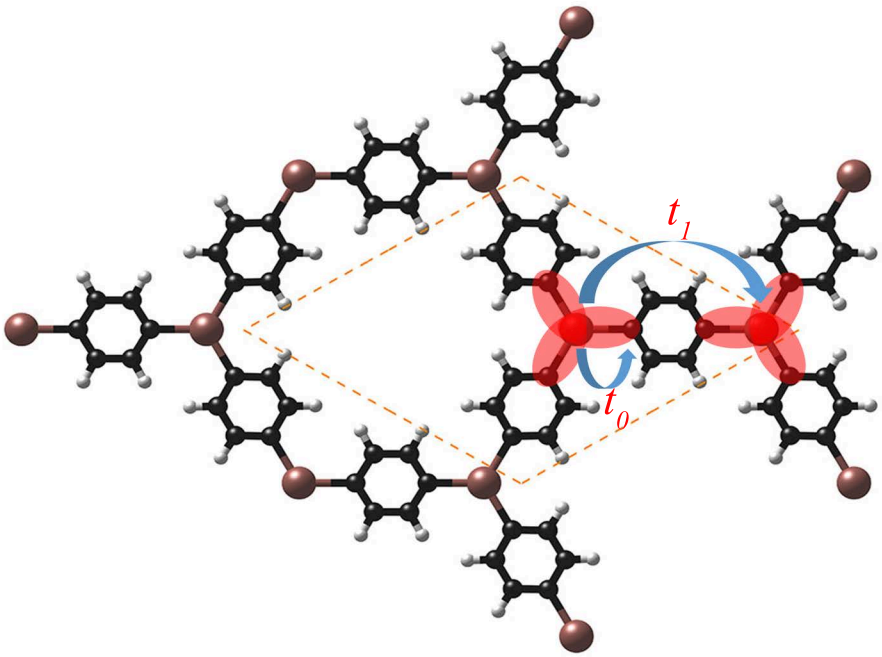

Figure 5.1. Atomic structure of the Tl_2Ph_3 lattice. The dashed yellow lines show the unit cell.

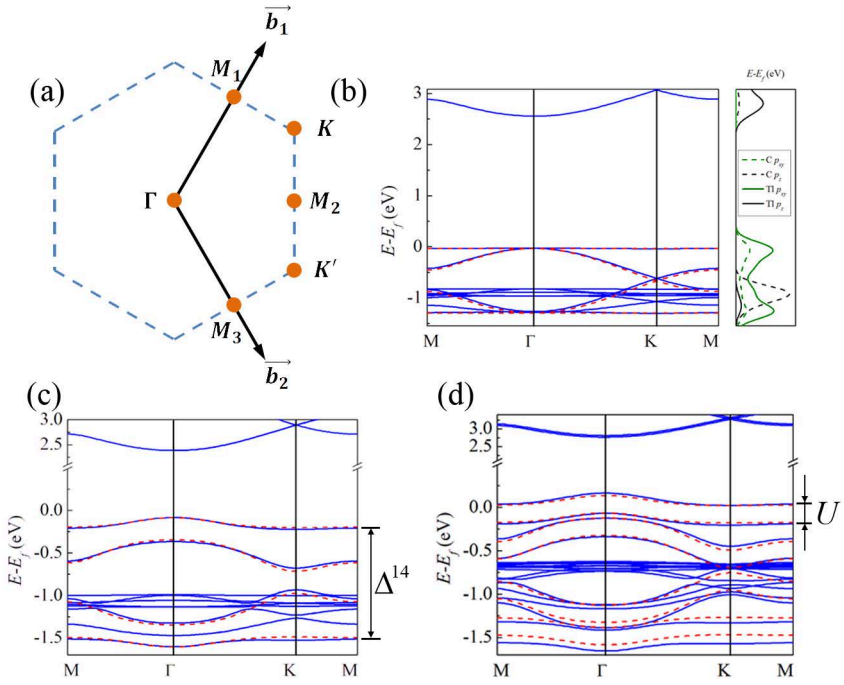

Figure 5.2. Band structure of the Tl_2Ph_3 lattice. (a)The first Brillouin zone and high symmetry points. (b) Band structure and atomic-orbital projected DOS of the Tl_2Ph_3 lattice without SOC. (c) Band structure with SOC. (d) band structure with SOC and one hole doped per unit cell. The blue solid lines represent our first principles results and the red dashed lines are results from the tight banding model (Eqs. 5.9) with parameters: (a) t_1=0.63; (b) t_1=0.63, λ=0.05 eV; (c) t_1=0.63 eV, λ=0.13 eV and M=0.1 eV.

spin degenerated due to the time-reversal and inversion symmetry.

Because of the large DOS at the Fermi level of the partially filled flat band, even an arbitrarily small Coulomb interaction will drive the system into a ferromagnetic ground state at specific filling factors [17,18]. We can separate the spin-up and spin-down bands by simply introducing one hole into the unit cell, while maintaining the charge neutrality with a compensating homogenous background charge. Figure 5.2d shows the band structure of the hole-doped Tl_2Ph_3 lattice. The degenerated spin-up and spin-down components are split, with the Fermi level aligns in between the spin-polarized flat bands. The total energy of Tl_2Ph_3 lattice in ferromagnetic ground state is 30 meV lower than that in the spin-unpolarized state. And as discussed in Ref [13], external Zeeman field can provide additional stabilization to the ferromagnetic Tl_2Ph_3 lattice. The spin splitting U is about 228 meV, which represents the strength of the on-site Coulomb interaction. We reiterate in Table 5.1 several key energy scales associated with the FCB in the Tl_2Ph_3 lattice and compare them with the results of the IPOF [13].

Now, we will check the edge states of a semi-infinite Tl_2Ph_3 lattice by calculating the momentum-resolved edge DOS because the number of chiral edge modes circulating around the boundary is an important signature of the nontrivial flat band. We calculated the edge states by using the Wannier90 package [19], in which a tight binding (TB) Hamiltonian in the basis of the maximally localized Wannier functions (MLWFs) is fitted to the first-principles band structures. Using these MLWFs, the edge Green's function of the semi-infinite lattice is constructed using the recursive method [20], and the local density of state (LDOS) of the edge is calculated. This method provides a direct connectivity between the edge states and the bulk states. The LDOS of a semi-infinite Tl_2Ph_3 is shown in Figure 5.3b and c for spin-up and spin-down components, respectively, where one can see the nontrivial topological edge states that connect the bulk states and form a 1D Dirac cone in both SOC

Table 5.1. Comparison of some energy scales between Tl_2Ph_3 lattice and IPOF system

Property	Symbol	Value in Tl_2Ph_3 lattice	Value in IPOF system [13]
Bandwidth	W	140 meV(Figure 5.3a)	60 meV
Spin splitting	U	228 meV(Figure 5.2d)	100 meV
Energy gap	Δ^{12}_{dir}	284 meV(Figure 5.3a)	90 meV
	Δ^{12}_{ind}	143 meV(Figure 5.3a)	30 meV
	Δ^{23}	255 meV(Figure 5.3a)	N/A
	Δ^{14}	1.3 eV(Figure 5.2c)	1.4 eV

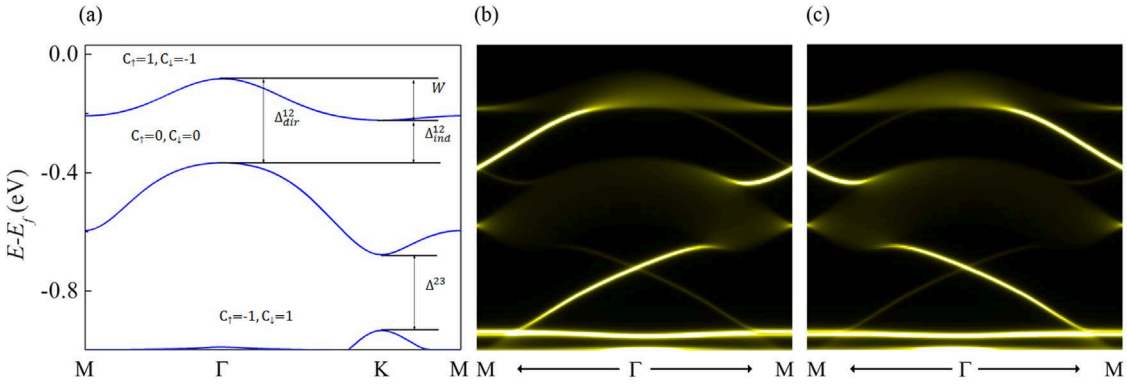

Figure 5.3. Evidences of topological states in the Tl_2Ph_3 lattice. (a) Band structure of Tl_2Ph_3 lattice near Fermi level. (b and c) The semi-infinite edge states for the spin-up and spin-down components, respectively. Overlapping these two figures would give the 1D edge Dirac band in both SOC gaps.

gaps (Δ^{12} and Δ^{23}).

To further confirm the nontrivial topology of the Tl_2Ph_3 lattice, the Chern number (C) and spin Chern number (C^s) are calculated using Kubo formula [21,22] as follows:

$$C = \frac{1}{2\pi}\int_{BZ} \mathrm{d}^2\overrightarrow{k}\,\Omega(\overrightarrow{k}) \tag{5.1}$$

$$\Omega(\overrightarrow{k}) = \sum_n f_n \Omega_n(\overrightarrow{k}) \tag{5.2}$$

$$\Omega_n(\overrightarrow{k}) = -\sum_{n'\neq n} 2\,\mathrm{Im}\,\frac{\langle\Psi_{nk} \mid \nu_x \mid \Psi_{n'k}\rangle\langle\Psi_{n'k} \mid \nu_y \mid \Psi_{nk}\rangle}{(\varepsilon_{n'k} - \varepsilon_{nk})^2} \tag{5.3}$$

$$C^s = \frac{1}{2\pi}\int_{BZ} \mathrm{d}^2\overrightarrow{k}\,\Omega^s(\overrightarrow{k}) \tag{5.4}$$

$$\Omega^s(\overrightarrow{k}) = \sum_n f_n \Omega^s_n(\overrightarrow{k}) \tag{5.5}$$

$$\Omega^s_n(\overrightarrow{k}) = -\sum_{n'\neq n} 2\,\mathrm{Im}\,\frac{\langle\Psi_{nk} \mid j_x \mid \Psi_{n'k}\rangle\langle\Psi_{n'k} \mid \nu_y \mid \Psi_{nk}\rangle}{(\varepsilon_{n'k} - \varepsilon_{nk})^2} \tag{5.6}$$

where n is the band index, Ψ_{nk} are the eigenstate of eigenvalue ε_{nk} of band n, f_n is the Fermi distribution function, $\nu_{x/y}$ is the velocity operator, j_x is the spin current operator defined as $(s_z\nu_x + \nu_x s_z)/2$, and s_z is the spin operator. The Chern number and spin Chern number are defined as

$$C = C_\uparrow + C_\downarrow \quad C^s = \frac{1}{2}(C_\uparrow - C_\downarrow) \tag{5.7}$$

From Eqs. 5.1-5.7, the Chern number of each band with different spins is calculated, as marked in Figure 5.3a. For both spins, the top flat band and the lower Dirac band

have a nonzero Chern number (±1), while the upper Dirac band has a zero Chern number. As a consequence, within the SOC gap of Δ^{12} and Δ^{23}, the Chern number is zero, but the spin Chern number is -1, which demonstrates that the Tl_2Ph_3 lattice is topologically nontrivial. The coexistence of two TI states, one from the Dirac band and the other from the topmost flat band, at different energies can manifest in transport measurement. The spin Hall conductance can be obtained from the spin Chern number as

$$\sigma_{xy}^{SH} = \frac{e}{4\pi}(C_{\uparrow} - C_{\downarrow}) \tag{5.8}$$

Figure 5.4a shows the calculated spin Hall conductance as a function of energy using the first-principles method, which has a quantized value (-2e/4π) within the energy window of both SOC gaps.

The four bands of the Tl_2Ph_3 lattice can be described by using the same tight-binding model proposed for IPOF [13], from which we can obtain a better understanding about the FCB in the Tl_2Ph_3 lattice. The corresponding effective Hamiltonian can be expressed as follows:

$$H = \begin{pmatrix} 0 & 0 & V_{xx} & V_{xy} \\ 0 & 0 & V_{xy} & V_{yy} \\ V_{xx}^* & V_{xy}^* & 0 & 0 \\ V_{xy}^* & V_{yy}^* & 0 & 0 \end{pmatrix} + \sigma_z\lambda \begin{pmatrix} 0 & -i & 0 & 0 \\ i & 0 & 0 & 0 \\ 0 & 0 & 0 & -i \\ 0 & 0 & -i & 0 \end{pmatrix} + \sigma_z M \tag{5.9}$$

in which $\sigma_z = \pm 1$ is the spin eigenvalue, $V_{xx} = \frac{1}{2}(1 + e^{i\mathbf{k}\cdot\mathbf{a_1}})$, $V_{xy} = \frac{\sqrt{3}}{6}(1 - e^{i\mathbf{k}\cdot\mathbf{a_1}})$, and $V_{yy} = \frac{1}{\sqrt{6}}(1 + e^{i\mathbf{k}\cdot\mathbf{a_1}} + 4e^{i\mathbf{k}\cdot\mathbf{a_2}})$; $\mathbf{a_{1,2}}$ is the lattice vector. There are three parameters in the model: the next-nearest-neighbor (NNN) hopping parameter t_1, the spin-orbit coupling strength λ, and the spontaneous magnetization M. By fitting the three parameters to the DFT results, the dispersion of the four p_{xy} bands can be well reproduced, as is shown in Figure 5.2b, c, and d. The TB model analysis indicates that the SOC gaps (Δ^{12} and Δ^{23}) in the Tl_2Ph_3 lattice are opened due to the intrinsic SOC of p_{xy} orbitals of Tl atoms, given the inversion lattice symmetry that excludes the Rashba SOC effect.

5.4 Conclusion

In conclusion, we predicted the existence of a flat band with topological quantum number around Fermi level in a 2D organometallic framework. Our study indicates that the Tl_2Ph_3

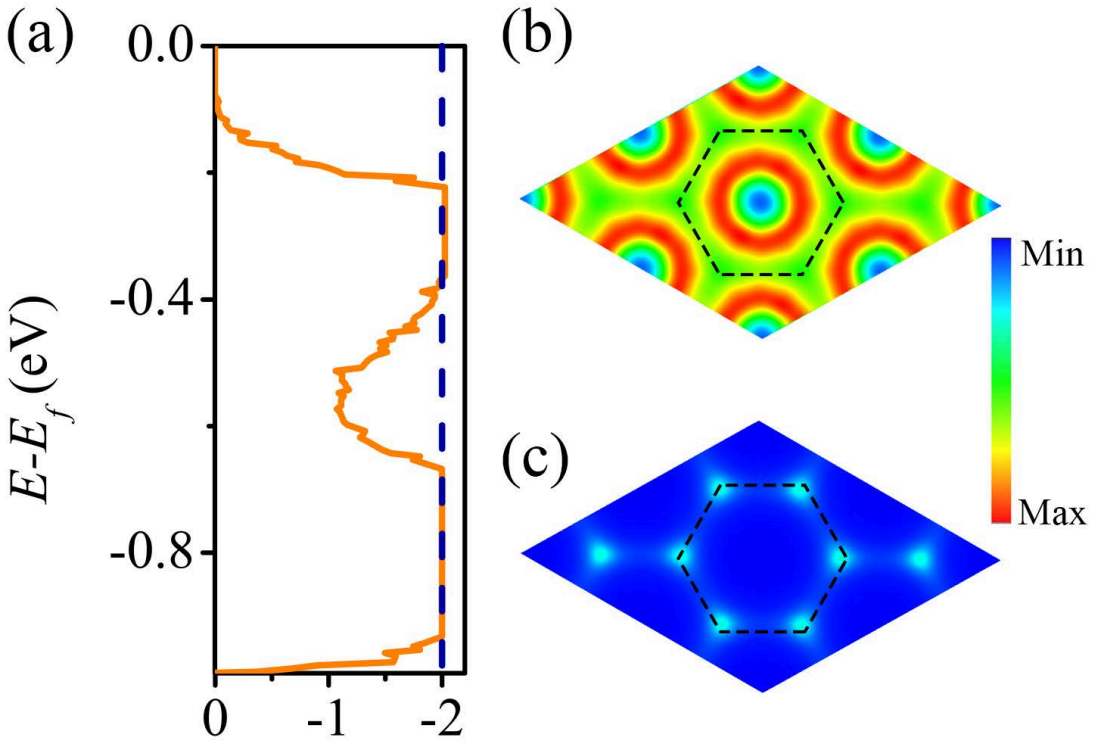

Figure 5.4. Hall conductance and the Berry phase in the Tl_2Ph_3 lattice. (a) Quantized spin Hall conductance within the energy window of the two SOC gaps. (b and c) Spin Berry curvatures in the reciprocal space for flat (b) and Dirac bands (c). The dashed line marks the first Brillouin zone.

lattice has the largest SOC gap among all the OTIs proposed so far [1113,23], which is comparable to that in typical large gap inorganic topological insulator [24,25]. The flat and Dirac bands are mainly originated from p_{xy} orbitals of Tl atoms and the SOC between the p_{xy} orbits result in the large SOC gap. Our findings proved the potential for measurement of topological edge states of 2D OTI at room temperature and could accelerate the experimental search for OTIs.

5.5 Reference

[1] T. Neupert, L. Santos, C. Chamon, and C. Mudry, Phys. Rev. Lett. **106**, 236804 (2011).

[2] K. Sun, Z. Gu, H. Katsura, and S. Das Sarma, Phys. Rev. Lett. **106**, 236803 (2011).

[3] E. Tang, J.-W. Mei, and X.-G. Wen, Phys. Rev. Lett. **106**, 236802 (2011).

[4] A. K. Geim, Rev. Mod. Phys. **83**, 851 (2011).

[5] K. S. Novoselov, Rev. Mod. Phys. **83**, 837 (2011).

[6] M. Z. Hasan and C. L. Kane, Rev. Mod. Phys. **82**, 3045 (2010).

[7] X.-L. Qi and S.-C. Zhang, Rev. Mod. Phys. **83**, 1057 (2011).

[8] D. Sheng, Z.-C. Gu, K. Sun, and L. Sheng, Nat. Commun. **2**, 389 (2011).

[9] J. W. F. Venderbos, M. Daghofer, and J. van den Brink, Phys. Rev. Lett. **107**, 116401 (2011).

[10] Y.-F. Wang, Z.-C. Gu, C.-D. Gong, and D. N. Sheng, Phys. Rev. Lett. **107**, 146803 (2011).

[11] Z. Wang, Z. Liu, and F. Liu, Nat. Commun. **4**, 1471 (2013).

[12] Z. F. Wang, Z. Liu, and F. Liu, Phys. Rev. Lett. **110**, 196801 (2013).

[13] Z. Liu, Z.-F. Wang, J.-W. Mei, Y.-S. Wu, and F. Liu, Phys. Rev. Lett. **110**, 106804 (2013).

[14] G. Kresse and J. Hafner, Phys. Rev. B **47**, 558 (1993).

[15] O. Ourdjini, R. Pawlak, M. Abel, S. Clair, L. Chen, N. Bergeon, M. Sassi, V. Oison, J.-M. Debierre, R. Coratger, and L. Porte, Phys. Rev. B **84**, 125421 (2011).

[16] N. A. A. Zwaneveld, R. Pawlak, M. Abel, D. Catalin, D. Gigmes, D. Bertin, and L. Porte, J. Am. Chem. Soc. **130**, 6678 (2008).

[17] A. Mielke, J. Phys. A **24**, L73 (1991).

[18] A. Mielke, J. Phys. A **24**, 3311 (1991).

[19] A. A. Mostofi, J. R. Yates, Y.-S. Lee, I. Souza, D. Vanderbilt, and N. Marzari, Comput. Phys. Commun. **178**, 685 (2008).

[20] M. L. Sancho, J. L. Sancho, J. L. Sancho, and J. Rubio, J. Phys. F **15**, 851 (1985).

[21] Y. Yao and Z. Fang, Phys. Rev. Lett. **95**, 156601 (2005).

[22] Y. Yao, L. Kleinman, A. H. MacDonald, J. Sinova, T. Jungwirth, D. Wang, E. Wang, and Q. Niu, Phys. Rev. Lett. **92**, 037204 (2004).

[23] Z. Wang, N. Su, and F. Liu, Nano Lett. **13**, 2842 (2013).

[24] C. Si, J. Liu, Y. Xu, J. Wu, B.-L. Gu, and W. Duan, arXiv:**1401**.4100.

[25] Y. Xia, D. Qian, D. Hsieh, L. Wray, A. Pal, H. Lin, A. Bansil, D. Grauer, Y. Hor, R. Cava, and others, Nat. Phys. **5**, 398 (2009).